

1 **Energetic constraints on the pattern of changes to the hydrological cycle**
2 **under global warming**

3 David B. Bonan,^a Nicholas Siler,^b Gerard H. Roe,^c Kyle C. Armour,^c

4 ^a *California Institute of Technology, Pasadena, California, USA*

5 ^b *Oregon State University, Corvallis, Oregon, USA*

6 ^c *University of Washington, Seattle, Washington, USA*

7 *Corresponding author:* David B. Bonan, dbonan@caltech.edu

8 ABSTRACT: The response of precipitation minus evaporation ($P - E$) to global warming is inves-
9 tigated using a moist energy balance model (MEBM) with a simple Hadley-Cell parameterization.
10 The MEBM accurately emulates $P - E$ changes simulated by a suite of global climate models
11 (GCMs) under greenhouse-gas forcing. The MEBM also accounts for most of the intermodel
12 differences in GCM $P - E$ changes and better emulates GCM $P - E$ changes when compared to
13 the “wet-gets-wetter, dry-gets-drier” thermodynamic mechanism. The intermodel spread in $P - E$
14 changes are attributed to intermodel differences in radiative feedbacks, which account for 60 – 70%
15 of the intermodel variance, with smaller contributions from radiative forcing and ocean heat uptake.
16 Isolating the intermodel spread of feedbacks to specific regions shows that tropical feedbacks are
17 the primary source of intermodel spread in $P - E$ changes. The ability of the MEBM to emulate
18 GCM $P - E$ changes is further investigated using idealized feedback patterns. A less negative and
19 narrowly peaked feedback pattern near the equator results in more atmospheric heating, which
20 strengthens the Hadley Cell circulation in the deep tropics through an enhanced poleward heat
21 flux. This pattern also increases gross moist stability, which weakens the subtropical Hadley Cell
22 circulation. These two processes in unison increase $P - E$ in the deep tropics, decrease $P - E$ in the
23 subtropics, and narrow the Intertropical Convergence Zone. Additionally, a feedback pattern that
24 produces polar-amplified warming reduces the poleward moisture flux by weakening the merid-
25 ional temperature gradient and the Clausius-Clapeyron relation. It is shown that changes to the
26 Hadley Cell circulation and the poleward moisture flux are crucial for understanding the pattern of
27 GCM $P - E$ changes under warming.

28 SIGNIFICANCE STATEMENT: Changes to the hydrological cycle over the 21st century are
29 predicted to impact ecosystems and socioeconomic activities throughout the world. While it is
30 broadly expected that dry regions will get drier and wet regions will get wetter, the magnitude
31 and spatial structure of these changes remains uncertain. In this study, we use an idealized
32 climate model, which makes an assumption about how energy is transported in the atmosphere, to
33 understand the processes setting the pattern of precipitation and evaporation under global warming.
34 We first use the idealized climate model to explain why comprehensive climate models predict
35 different magnitudes of precipitation and evaporation across a range of latitudes. We show this
36 arises primarily from climate feedbacks, which act to amplify or dampen the amount of warming.
37 Ocean heat uptake and radiative forcing play secondary roles, but can account for a significant
38 amount of the uncertainty in regions where ocean circulation influences the rate of warming. We
39 further show that uncertainty in tropical feedbacks (mainly from clouds) affects changes to the
40 hydrological cycle across a range of latitudes. We then show how the pattern of climate feedbacks
41 affects how the patterns of precipitation and evaporation respond to climate change through a
42 set of idealized experiments. These results show how the pattern of climate feedbacks impacts
43 tropical hydrological changes by affecting the strength of the Hadley circulation and impacts polar
44 hydrological changes through changes in the transport of moisture to the high latitudes.

45 1. Introduction

46 The hydrological cycle, which describes the continuous movement of water on Earth, is a key
47 component of the climate system. A fundamental measure of the hydrological cycle is the net
48 water flux into the surface, which is equal to the difference between precipitation and evaporation
49 ($P - E$). The magnitude and spatial pattern of $P - E$ affects the formation of water masses in the
50 ocean (e.g., Schmitt et al. 1989; Large and Nurser 2001; Abernathy et al. 2016; Groeskamp et al.
51 2019), the salinity and stratification of the ocean's mixed layer (e.g., de Boyer Montégut et al.
52 2007), and the amount of runoff or availability of water over the land (e.g., Dai and Trenberth
53 2002; Field and Barros 2014). $P - E$ can also modulate transient climate change through changes
54 in upper-ocean salinity, which impacts the degree of ocean heat uptake by changing the vertical
55 stratification of the ocean (e.g., Liu et al. 2021). The magnitude and spatial pattern of $P - E$ has
56 been dramatically different in past climate states (e.g., Winguth et al. 2010; Boos 2012; Carmichael

57 et al. 2016) and is predicted to change substantially over the next century (e.g., Mitchell et al. 1987;
 58 Chou and Neelin 2004; Held and Soden 2006; Byrne and O’Gorman 2015; Siler et al. 2018).

59 In response to increased greenhouse-gas concentrations, state-of-the-art global climate models
 60 (GCMs) consistently predict enhanced tropical precipitation and reduced subtropical precipitation
 61 over the 21st century. As noted by Held and Soden (2006), this “wet gets wetter, dry gets drier”
 62 paradigm can be understood by assuming that the change in $P - E$ with warming is due primarily
 63 to the change in moisture content of the atmosphere, with little contribution from changes in
 64 atmospheric circulations. A simple scaling for these changes can be derived from the fact that
 65 on climatological time scales, $P - E$ is equal to the convergence of the mass-weighted, vertically
 66 integrated moisture flux F_L :

$$P - E = -\nabla \cdot F_L. \quad (1)$$

67 As discussed in Held and Soden (2006) (hereafter referred to as HS06), an approximation for
 68 the change in $P - E$ under warming can be obtained by assuming the change in F_L is dominated
 69 by the change in lower-tropospheric specific humidity, with no changes in relative humidity and
 70 atmospheric circulation. These constraints mean that, as the atmosphere warms, F_L will increase
 71 at close to the Clausius-Clapeyron rate, implying that:

$$F'_L \approx \alpha T' F_L, \quad (2)$$

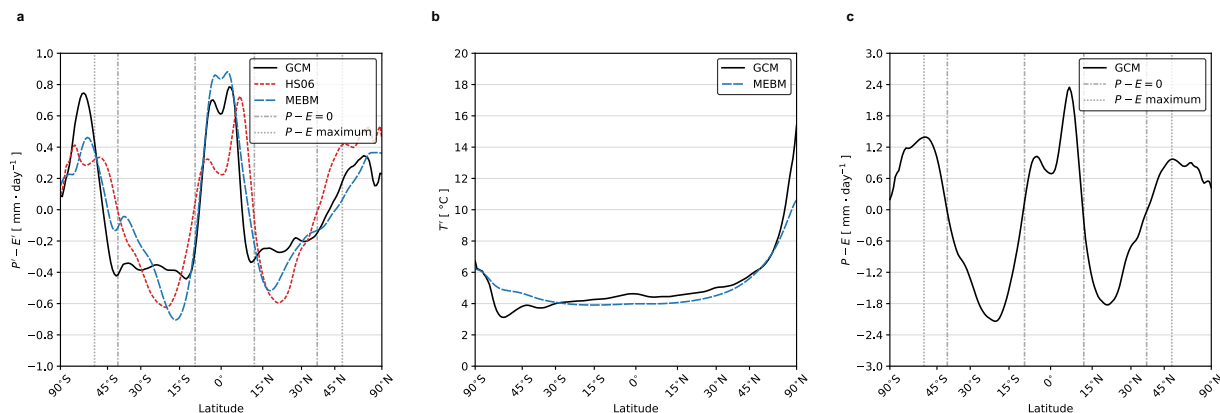
72 where primes indicate the difference between the perturbed and control climates; and:

$$\alpha = \frac{L_v}{R_v T^2}, \quad (3)$$

73 is the Clausius-Clapeyron scaling factor, where L_v is the latent heat of vaporization, R_v is the
 74 gas constant of water vapor, and T is the near-surface air temperature. For typical atmospheric
 75 temperatures, α ranges from around 6 % K⁻¹ (when $T = 30^\circ\text{C}$) to more than 9 % K⁻¹ (when
 76 $T = -30^\circ\text{C}$). If one assumes that gradients in α and T' are relatively small, Eq. (1) implies that the
 77 change in $P - E$ under warming will also scale at the Clausius-Clapeyron rate, which results in:

$$P' - E' \approx \alpha T' (P - E). \quad (4)$$

78 Eq. (4) implies that a spatially uniform increase in precipitable water will enhance the existing
 79 pattern of $P - E$: increasing $P - E$ in the tropics and high latitudes and decreasing $P - E$ in the
 80 subtropics under global warming (e.g., Chou and Neelin 2004; Emori and Brown 2005; Held and
 81 Soden 2006; Seager et al. 2010). Eq. (4) also implies that the climatological boundaries of where
 82 $P - E = 0$ will remain fixed.



83 **FIG. 1. Response of the hydrological cycle to global warming.** (a) The multi-model mean change in zonal-
 84 mean precipitation minus evaporation ($P' - E'$) from 20 CMIP5 simulations 126 – 150 years after an abrupt
 85 quadrupling of CO_2 relative to the pre-industrial average (black). The HS06 approximation (red densely dashed
 86 line) is calculated from Eq. (4) and found by applying the multi-model mean zonal-mean change in near-surface
 87 air temperature from the abrupt quadrupling of CO_2 (black line in panel b) and the multi-model mean $P - E$
 88 climatology from the preindustrial-control simulations (panel c) assuming $\alpha = 7 \text{ \% K}^{-1}$ globally. The blue
 89 line shows the MEBM $P' - E'$ pattern (which is described in Section 2). (b) The multi-model mean change in
 90 zonal-mean near-surface air temperature (T') of (black) 20 CMIP5 GCMs and (blue line) the MEBM temperature
 91 change (see Section 2). (c) The climatology of multi-model mean zonal-mean precipitation minus evaporation
 92 ($P - E$) of 20 CMIP5 GCMs. The grey dashed vertical lines in (a) and (c) represent the climatological $P - E = 0$
 93 in preindustrial-control simulations, which corresponds to the subtropical regions; and the grey dotted vertical
 94 lines represent the climatological $P - E$ maximum in preindustrial-control simulations, which is a measure of
 95 the latitude of the storm tracks.

96 HS06 found that Eq. (4) broadly captured the spatial structure of $P' - E'$ as simulated by coupled
 97 GCMs under rising greenhouse-gas concentrations. Figure 1a shows the multi-model mean pattern
 98 of $P' - E'$ averaged over years 126 – 150 after an abrupt quadrupling of CO_2 ($4 \times \text{CO}_2$) for 20 GCMs
 99 participating in phase 5 of the Coupled Model Intercomparison Project (CMIP5). Under global

100 warming, GCMs show increasing $P - E$ in the tropics and high latitudes and decreasing $P - E$ in
101 the subtropics (see black line in Fig. 1a). The red dashed line shows the HS06 approximation from
102 Eq. (4) using the multi-model mean patterns of T' (Fig. 1b) and $P - E$ (Fig. 1c) from the same
103 20 GCMs, assuming that $\alpha = 7\% \text{ K}^{-1}$ everywhere. While the approximation indeed captures the
104 overall spatial pattern of $P' - E'$ in GCM simulations of global warming, there are a few aspects
105 that are not captured. Namely, Eq. (4) predicts $P - E$ changes that are too large in the Northern
106 Hemisphere extratropics and in the subtropical regions of both hemispheres, and predicts $P - E$
107 changes that are too small in the tropics and the Southern Hemisphere extratropics. Furthermore,
108 Eq. (4) does not capture other robust features of $P - E$ changes as seen in GCMs, such as the
109 poleward expansion of the subtropics (defined by the boundary of where $P - E = 0$; Lu et al.
110 2007; Kang and Lu 2012), a poleward shift of the $P - E$ maximum associated with the midlatitude
111 storm tracks (Lu et al. 2010; Chang et al. 2012; Mbengue and Schneider 2013, 2017, 2018), and a
112 contraction of the Inter-tropical Convergence Zone (ITCZ; Byrne and Schneider 2016b).

113 Some of the differences between the patterns of $P' - E'$ predicted by Eq. (4) and simulated
114 by GCMs have been reconciled through additional terms that account for the spatial pattern of
115 temperature change or changing atmospheric circulations. For instance, Boos (2012) showed
116 that including the pattern of temperature change is necessary for understanding $P - E$ changes
117 at the Last Glacial Maximum, where ice sheets greatly altered horizontal temperature gradients.
118 Similarly, Byrne and O’Gorman (2015) showed that changes to the patterns of temperature and
119 relative humidity are important when considering the response of $P - E$ to warming over land,
120 where warming is generally amplified and relative humidity generally decreases. However, these
121 modifications to the HS06 approximation are still fundamentally thermodynamic, and do not
122 account for the potential impact of dynamical changes on the pattern of $P - E$. Other studies have
123 shown that changing atmospheric circulations play an important role in determining the degree of
124 subtropical expansion and narrowing of the ITCZ (Seager et al. 2010; Seager and Vecchi 2010), as
125 well as poleward shifts in the mid-latitude storm tracks (Scheff and Frierson 2012).

126 More recently, Siler et al. (2018) simulated the change in zonal-mean $P - E$ using a moist
127 energy balance model (MEBM) with a simple Hadley Cell parameterization, which transports
128 latent energy diffusively down-gradient in the mid- to high-latitudes but allows for latent energy
129 to travel up-gradient in the tropics. Siler et al. (2018) showed that the MEBM accurately emulates

130 $P - E$ changes as simulated by comprehensive GCMs under global warming (see blue dashed line
131 in Fig. 1a). In particular, the MEBM correctly simulates the larger increase in $P - E$ in the deep
132 tropics and more muted $P - E$ changes in the Northern Hemisphere extratropics (Fig. 1a). As
133 noted above, GCMs predict an expansion of the subtropics both equatorward and poleward, which
134 can be seen in Fig. 1a. The dash-dot vertical lines denote where $P - E = 0$ in the climatology. Note
135 that regions where $P' - E'$ in the MEBM are negative extends across the vertical lines, indicating
136 a narrowing of the ITCZ and an expansion of the subtropics. Likewise, the dotted vertical lines in
137 Fig. 1a denote the location of maximum $P - E$ in the climatology, and a similar comparison with
138 $P' - E'$ shows that there is a poleward shift in the maximum $P - E$. Siler et al. (2018) argued that
139 polar amplification — which is a robust feature of global warming — affects $P' - E'$ by weakening
140 the temperature dependence of the Clausius-Clapeyron relation and also decreasing the poleward
141 moisture transport. This helps to explain why there is reduced high-latitude $P - E$ changes and
142 why the subtropical regions expand under warming in the MEBM and GCMs. However, it is still
143 unclear why the pattern of $P' - E'$ from the MEBM is in better agreement with GCMs than Eq.
144 (4) in the deep tropics, capturing increasing $P - E$ in the deep tropics and a narrowing of the ITCZ
145 region (Fig. 1a). Indeed, large-scale circulation features like the Hadley Cells dominate latent
146 energy transport in the deep tropics. This leads to a key question: How important are changes to
147 the strength of the Hadley Cells for $P - E$ changes in the tropics? Previous work (e.g., Byrne and
148 Schneider 2016a,b) has shown that energetic arguments can be invoked to understand processes
149 contributing to a narrowing of the ITCZ, but it remains unclear what energetic processes are driving
150 these circulation changes and how these circulation changes relate to $P - E$ changes.

151 Better understanding processes that set the pattern of $P' - E'$ may also help reduce uncertainty in
152 future precipitation projections as sources of intermodel spread can be identified. Current GCMs
153 exhibit a large intermodel spread in the pattern of $P' - E'$ under global warming, and the exact
154 reason for this spread remains unknown (Prein and Pendergrass 2019). Previous studies have
155 shown that tropical radiative feedbacks contribute to uncertainty in the amount warming that is
156 nearly spatially uniform, while polar radiative feedbacks contribute to uncertainty in the amount
157 of warming that is confined to the poles (Roe et al. 2015; Bonan et al. 2018). Yet, an important
158 question remains unanswered: What processes constitute the greatest sources of uncertainty in the
159 pattern of $P' - E'$ under climate change? The ability of the MEBM to emulate the pattern of $P' - E'$

160 simulated by GCMs under greenhouse-gas forcing (see Fig. 1a) suggests the MEBM can also be
161 used to examine drivers of uncertainty in $P' - E'$.

162 In this paper, we have two specific aims:

- 163 1. We identify sources of intermodel spread in the pattern of $P' - E'$ under global warming.
164 To do this, we first show that the MEBM is able to account for a majority of the intermodel
165 variance in $P' - E'$ across a range of latitudes for GCMs under $4 \times \text{CO}_2$. We then link the
166 intermodel spread in $P' - E'$ to radiative feedbacks, radiative forcing, and ocean heat uptake.
- 167 2. We further investigate differences between the simple thermodynamic perspective introduced
168 by HS06 and the downgradient energy transport perspective introduced by Siler et al. (2018).
169 Specifically, we use the MEBM to consider how the pattern of radiative feedbacks impacts
170 the pattern of $P' - E'$ in the tropical and extratropical polar regions. We show that changes to
171 the net heating of the atmosphere act to strengthen the Hadley Cell, which increases moisture
172 transport to the tropics, producing a narrowing of the ITCZ and increasing $P - E$ in the deep
173 tropics. We also show how the meridional temperature gradient alters poleward moisture
174 transport.

175 The paper is structured as follows. In Section 2, we describe the MEBM and Hadley Cell
176 parameterization. In Section 3, we assess the skill of the MEBM in emulating GCMs under
177 greenhouse-gas forcing and use the MEBM to identify sources of uncertainty in the pattern of
178 $P' - E'$. In Section 4, we examine how the pattern of radiative feedbacks impacts $P - E$ changes
179 in the deep tropics and extratropics using a set of simple scalings and compare these results to
180 CMIP5. Finally, in Section 5, we discuss key results and implications of this work.

181 **2. A modified moist energy balance model**

182 A series of studies have shown that downgradient energy transport by the atmosphere is remark-
183 ably successful at emulating the zonal-mean climate, and its response to greenhouse-gas forcing
184 (Flannery 1984; Hwang and Frierson 2010; Roe et al. 2015; Siler et al. 2018; Bonan et al. 2018;
185 Merlis and Henry 2018; Armour et al. 2019; Russotto and Biasutti 2020; Lutsko et al. 2020; Hill
186 et al. 2020; Beer and Eisenman 2022). The MEBM assumes that the anomalous divergence of the
187 northward column-integrated atmospheric energy transport $F'(x)$ is proportional to the meridional

188 gradient of anomalous near-surface moist static energy $h' = c_p T' + L_v q'$, which gives:

$$F'(x) = \frac{2\pi p_s}{g} D (1-x^2) \frac{dh'}{dx}, \quad (5)$$

189 where c_p is the specific heat of air, q' is the anomalous near-surface specific humidity (assuming
 190 fixed relative humidity of 80%), p_s is surface air pressure (1000 hPa), g is the acceleration due to
 191 gravity (9.81 m s^{-2}), D is a constant diffusion coefficient (with units of $\text{m}^2 \text{ s}^{-1}$), x is sine latitude,
 192 and $1-x^2$ accounts for the spherical geometry.

193 Under warming, the anomalous heating of the atmosphere must be balanced by $F'(x)$. We define
 194 $R_f(x)$ as the local top-of-atmosphere (TOA) radiative forcing, $\lambda(x)$ as the local radiative feedback,
 195 defined as the change in net upward TOA radiative flux per degree of local surface warming (W
 196 $\text{m}^{-2} \text{ K}^{-1}$) and $G'(x)$ as the change in net surface heat flux, which is equivalent to the divergence
 197 of ocean heat transport and ocean heat storage. Combining these three terms (i.e., the anomalous
 198 heating of the atmosphere) with the divergence of Eq. (5) gives:

$$R_f(x) - G'(x) + \lambda(x)T'(x) = \nabla \cdot F'(x), \quad (6)$$

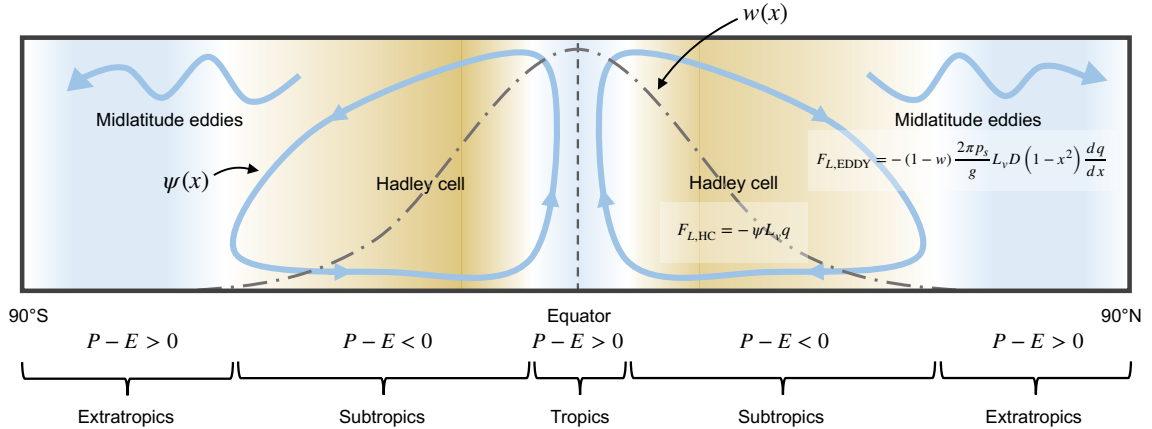
199 which is a single differential equation that can be solved numerically for $T'(x)$ and $F'(x)$ given
 200 patterns of $R_f(x)$, $G'(x)$, and $\lambda(x)$ and a value of D .

208 To simulate a realistic hydrological cycle, we follow Siler et al. (2018) and Armour et al.
 209 (2019) and define a Gaussian weighting function $w(x)$ that partitions the transport of anomalous
 210 latent and dry-static energy within the tropics. A schematic depicting the mean-state Hadley Cell
 211 parameterization is shown in Figure 2. Following Siler et al. (2018), we divide $F'(x)$ into a
 212 component due to the Hadley Cells $F'_{\text{HC}}(x)$ and a component due to the eddies $F'_{\text{EDDY}}(x)$, and
 213 define $w(x)$ as the fraction of total energy transport that is accomplished by the Hadley Cells at a
 214 given latitude:

$$F'_{\text{HC}}(x) = w(x)F'(x) \text{ and } F'_{\text{EDDY}}(x) = (1-w(x))F'(x), \quad (7)$$

215 and

$$w(x) = \exp\left(\frac{-x^2}{\sigma_x^2}\right), \quad (8)$$



201 **FIG. 2. Schematic depicting the Hadley Cell parameterization in the moist energy balance model.** A
 202 Gaussian weighting function $w(x)$, shown in the grey dash-dot line is used to partition atmospheric heat transport
 203 $F(x)$ into a component due to the Hadley Cell $F_{\text{HC}}(x)$ and a component due to mid-latitude eddies $F_{\text{EDDY}}(x)$. A
 204 streamfunction ψ is then approximated using assumptions about gross moist stability (see Section 2 and Appendix
 205 B). ψ is then used to flux moisture back up the meridional moist-static energy gradient while the rest is diffused
 206 down the meridional moist-static energy gradient and modulated by the weighting function. By summing the
 207 two terms and taking the divergence, a pattern of $P - E$ is obtained.

216 where σ_x is a width parameter, which we set to 0.30 following Siler et al. (2018). In this formulation,
 217 eddies account for essentially all anomalous energy transport poleward of 45°S and 45°N , while
 218 the Hadley Cell accounts for most anomalous energy transport between 10°S and 10°N . Note that
 219 this formulation explicitly leaves out representation of the extratropical components of the mean
 220 meridional circulation (i.e., Ferrel and polar cells) and does not allow for the extent of the Hadley
 221 Cell to change under warming (O’Gorman and Schneider 2008).

222 In the mean-state climate, poleward atmospheric heat transport by the Hadley Cell $F_{\text{HC}}(x)$ is
 223 equal to:

$$F_{\text{HC}}(x) = \psi(x)H(x), \quad (9)$$

224 where $\psi(x)$ is the mass transport (kg s^{-1}) in each branch of the Hadley Cell and $H(x)$ is the gross
 225 moist stability, defined as the difference between h in the upper and lower branches at each latitude
 226 (see details below). However, because we are considering $P - E$ changes under warming, the
 227 anomalous poleward atmospheric heat transport by the Hadley Cell is represented as:

$$F'_{\text{HC}}(x) = \psi'(x)\bar{H}(x) + \bar{\psi}(x)H'(x) + \psi'(x)H'(x), \quad (10)$$

228 where $\psi'(x)$ is the anomalous mass transport (kg s^{-1}) in each branch of the Hadley Cell and
 229 $H'(x)$ is the anomalous gross moist stability (i.e., the difference between h' in the upper and lower
 230 branches at each latitude). Note that we have written Eq. (10) in terms of a perturbation around the
 231 climatological mean-state. Appendix B details how the climatological state is approximated using
 232 the MEBM. In Section 3, we use the climatological state of each GCM. For the idealized analyses
 233 of Section 4, the climatological state is equivalent to the multi-model mean climatological state of
 234 the 20 CMIP5 GCMs under preindustrial conditions, but symmetric about the equator so as not to
 235 introduce hemispheric asymmetries.

236 Following Held (2001), we assume that anomalous upper tropospheric moist-static energy is
 237 uniform in the tropics with a constant value of h'_0 . Thus, variations in $H'(x)$ are due entirely to
 238 meridional variations in h' giving $H'(x) \approx h'_0 - h'(x)$, where $h'_0 = 1.08 \times h'(0)$, or 8% above h'
 239 at the equator ($x = 0$). Note that this value is slightly higher than the value used by Siler et al.
 240 (2018), which is 6% above h' at the equator, but was found to better emulate $P' - E'$ in GCMs. The
 241 anomalous latent energy transport by the Hadley Cell $F'_{L,\text{HC}}(x)$ is thus:

$$F'_{L,\text{HC}}(x) = - \left(\psi'(x)L_v\bar{q}(x) + \bar{\psi}(x)L_vq'(x) + \psi'(x)L_vq'(x) \right). \quad (11)$$

242 The assumption about moisture transport holds because the upper branch of the Hadley Cell is
 243 essentially dry, meaning anomalous latent energy transport is confined to the lower branch. With
 244 this simple Hadley Cell parameterization, the anomalous latent energy transport can be obtained
 245 by summing the term due to the Hadley Cells and the term due to mid-latitude eddies:

$$F'_L(x) = F'_{L,\text{HC}}(x) + F'_{L,\text{EDDY}}(x). \quad (12)$$

246 The divergence of $F'_L(x)$ (Eq. 12) then yields the change in $P - E$:

$$P' - E' = -\nabla \cdot F'_L(x) = -\frac{1}{2\pi a^2} \frac{dF'_L}{dx}. \quad (13)$$

247 This formulation of the MEBM enables us to examine how different factors, such as the patterns
248 of λ , G' , R_f , and T' impact that pattern of $P' - E'$.

249 3. Changes to the hydrological cycle in a moist energy balance model

258 We first assess the ability of the MEBM to emulate a suite of comprehensive GCMs under
259 greenhouse-gas forcing largely following Siler et al. (2018). To do this, we compute the model-
260 specific patterns of R_f , G' , and λ from 20 different CMIP5 GCMs (see Appendix A) and calculate
261 the $P' - E'$ pattern from the MEBM defined in Section 2. Note, for these analysis we use model-
262 specific values of D and climatological states from a climatological version of the MEBM (see
263 Appendix B).

264 Figure 3 shows the pattern of $P' - E'$ from each GCM, the MEBM solution, and the HS06
265 approximation. While the overall pattern of “wet gets wetter, dry gets drier” is similar across
266 both the HS06 approximation and MEBM, there is much better agreement between GCMs and
267 the MEBM than between GCMs and the HS06 approximation. For example, in GCMs with large
268 values of $P' - E'$ in the deep tropics (e.g., ACCESS-1.0, CanESM2, CSIRO-Mk3.6.0, and MIROC-
269 ESM) there is a good agreement between the MEBM and GCMs that is not captured by the HS06
270 approximation, suggesting that the MEBM is capturing changes in the strength of the Hadley Cell
271 circulation that the HS06 approximation leaves out. The MEBM also captures a narrowing of
272 the ITCZ region, which occurs in every GCM, and can be inferred from Fig. 3 because $P' - E'$
273 is negative at the equatorward climatological $P - E = 0$ line (dash-dot line in each panel). In the
274 extratropical regions, the MEBM captures the more muted $P - E$ changes also shown by GCMs
275 (e.g., ACCESS-1.3, CCSM4, HadGEM2-ES). The MEBM also broadly captures the expansion of
276 the subtropical regions in each GCM.

281 To quantitatively compare the pattern of $P' - E'$ from each individual GCM, the MEBM solution,
282 and the HS06 approximation, we take area-weighted averages of $P' - E'$ in five distinct regions that
283 represent the extratropical polar regions (90°S to 45°S and 45°N to 90°N), the subtropics (45°S to
284 10°S and 10°N to 45°N) and the deep tropics (10°S to 10°N). In the extratropical polar regions, the

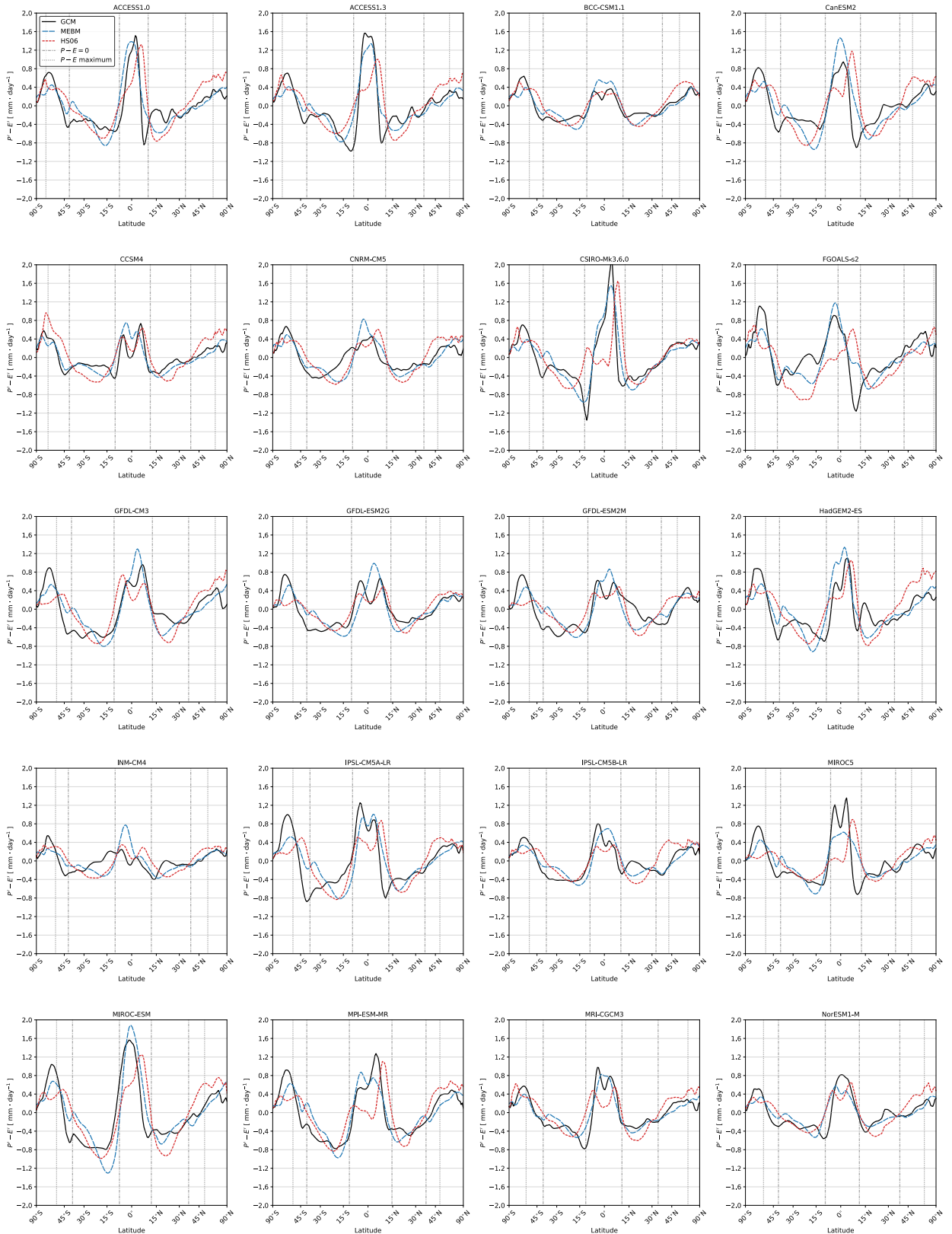
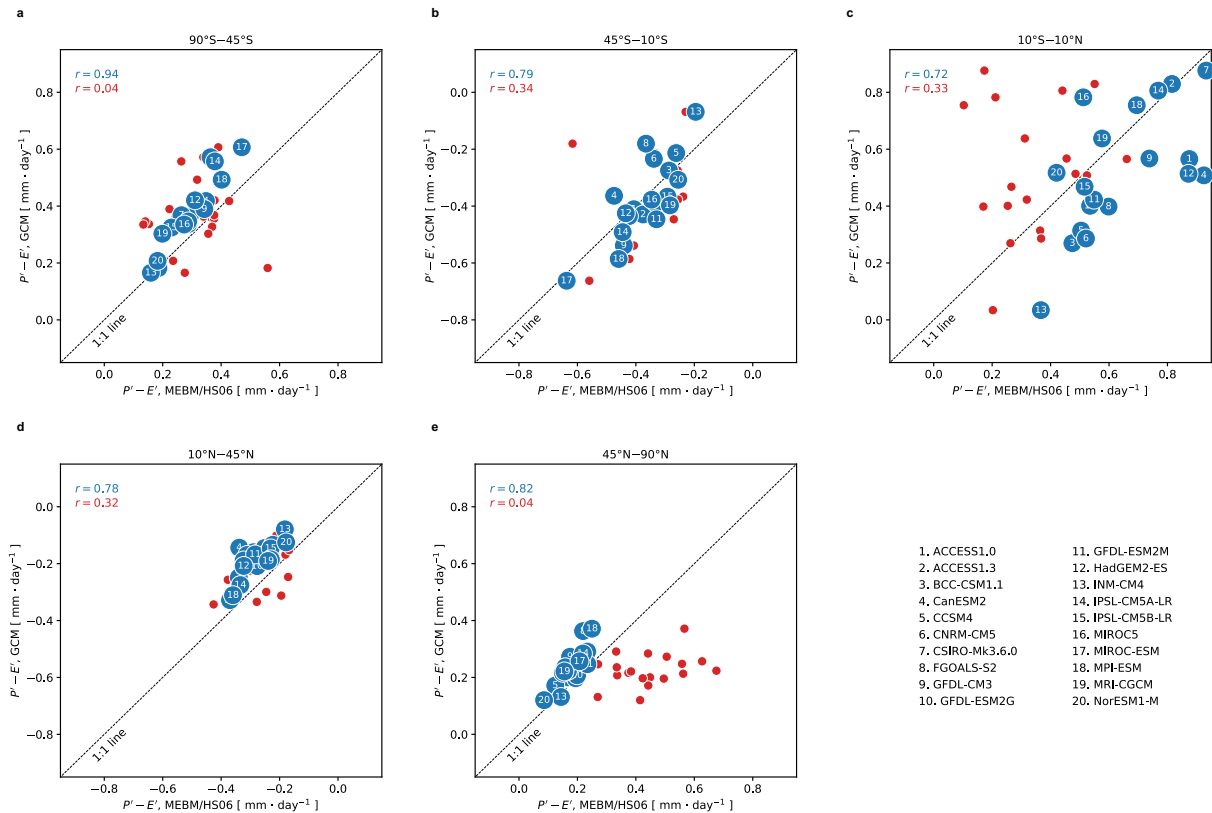


FIG. 3. See next page.

250 **FIG. 3. Response of the hydrological cycle to global warming in a moist energy balance model.** The
 251 pattern of $P' - E'$ in 20 CMIP5 simulations 126–150 years after an abrupt quadrupling of CO_2 . The black line
 252 denotes the GCM, the blue line denotes the MEBM solution, and the red line denotes the HS06 approximation.
 253 The grey line denotes an individual GCM or simulation and the colored line denotes the multi-model mean. The
 254 grey dashed vertical lines in (a) and (c) represent the $P - E = 0$ boundary in the climatology, which corresponds
 255 to the subtropical regions; and the grey dotted vertical lines represent the $P - E$ maximum, which is a measure
 256 of the latitude of the storm tracks. Changes in subtropical boundaries and stormtrack latitude can be inferred by
 257 comparing the $P' - E'$ changes with these vertical lines.

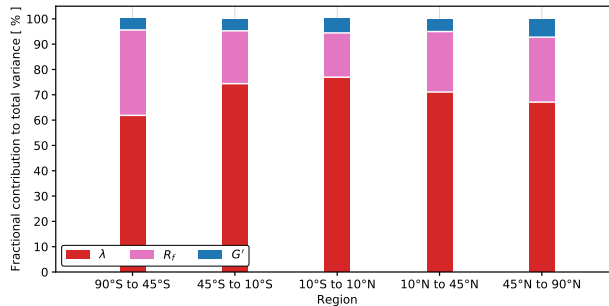


277 **FIG. 4. Skill of the moist energy balance model.** Scatter plots of the area-averaged $P' - E'$ in the GCM, Held
 278 and Soden (2006) approximation (red), and MEBM (blue) from (a) 90°S to 45°S, (b) 45°S to 10°S, (c) 10°S to
 279 10°N, (d) 10°N to 45°N, and (e) 45°N to 90°N. The top left corner of each plot shows the Pearson correlation
 280 coefficient between the $P' - E'$ responses from the MEBM and GCM (blue) and HS06 and GCM (red).

285 MEBM accounts for approximately 70% of the intermodel variance while the HS06 approximation
 286 accounts for none (Fig. 4a and 4e). In the subtropics, the MEBM accounts for less intermodel

287 variance ($r^2 \approx 0.60$; Fig. 4b and 4d), but still far more than the HS06 approximation ($r^2 \approx 0.10$). In
 288 the deep tropics, where the MEBM solution predicts larger increases in $P - E$ when compared to
 289 the HS06 approximation, the MEBM accounts for approximately 50% of the intermodel variance,
 290 compared with about 10% for the HS06 approximation (Fig. 4c).

291 *a. Sources of uncertainty*

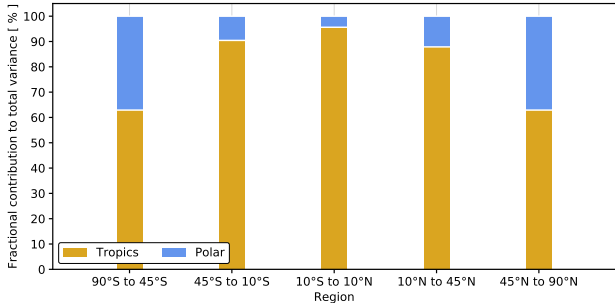


292 **FIG. 5. Sources of uncertainty in the response of the hydrological cycle to global warming in different**
 293 **regions.** Fractional contribution of λ , R_f , and G' to the total variance in $P' - E'$ for averages from 90°S to 45°S,
 294 45°S to 10°S, 10°S to 10°N, 10°N to 45°N, and 45°N to 90°N.

295 Having demonstrated that the MEBM emulates the pattern of $P' - E'$ for each individual GCM,
 296 we next investigate the reason for the good agreement between the MEBM and GCMs, and the
 297 intermodel spread of these $P' - E'$ patterns. Uncertainty in the MEBM mainly arises from three
 298 sources: radiative forcing R_f , ocean heat uptake G' , and radiative feedbacks λ . Following Bonan
 299 et al. (2018), we disaggregate the $P' - E'$ patterns into separate contributions from R_f , G' , and λ
 300 by creating a baseline pattern of $P' - E'$ for the MEBM using the multi-model mean patterns of
 301 R_f , G' , and λ . We then run the MEBM using the GCM-specific patterns of either R_f , G' , and λ
 302 (Figure A1) while holding the other two variables fixed at their multi-model mean patterns. This
 303 generates a spread of MEBM $P' - E'$ patterns due to intermodel differences in either R_f , G' , and
 304 λ . To understand the relative importance of each contributing factor, we calculate the variance
 305 of $P' - E'$ as a function of latitude from each individual factor. We then compute the fractional
 306 contribution of each factor to the total variance by assuming that the variance associated with each
 307 factor can be added linearly.

308 Figure 5 shows the fractional contribution of R_f , G' , and λ to the total variance in $P' - E'$ for the
 309 same regions described above. Across all regions intermodel variations in λ are the leading cause
 310 of intermodel variations in $P' - E'$, accounting for 60 – 75% of the intermodel variance. In the
 311 extratropical polar regions, the contribution of λ to the intermodel spread in $P' - E'$ is smaller than
 312 in the tropics (Fig. 5). R_f accounts for 15 – 30% of the intermodel variance in $P' - E'$ patterns,
 313 and accounts for more intermodel variance in the extratropical polar regions when compared to
 314 the tropics. Intermodel variations in G' account for 5 – 8% of the intermodel variance across all
 315 regions. Note that these averages represent broad swaths of $P' - E'$, which exhibits large spatial
 316 variations as a function of latitude. The same analysis as a continuous function of latitude yields a
 317 greater influence of G' at some latitudes, accounting for approximately 30 – 40% of the intermodel
 318 variance in $P' - E'$ in regions of large ocean heat uptake, like the North Atlantic and Southern
 319 Ocean.

320 *b. Local and remote impacts of climate feedbacks*



321 **FIG. 6. Local and remote influence of regional climate feedbacks on the response of the hydrological**
 322 **cycle to global warming.** Fractional contribution of intermodel variations of λ in the tropical (30°S to 30°N)
 323 and polar regions (90°S to 30°S and 30°N to 90°N) to the total variance in $P' - E'$ for averages from 90°S to
 324 45°S, 45°S to 10°S, 10°S to 10°N, 10°N to 45°N, and 45°N to 90°N.

325 Given that the intermodel spread of λ is the main source of uncertainty in the pattern of $P' - E'$, we
 326 next consider the relative importance of λ in different regions. The remote-versus-local influence
 327 of λ has been shown to be an important factor when considering uncertainty in the pattern of
 328 temperature (Roe et al. 2015; Bonan et al. 2018), but its influence on changes to $P' - E'$ is less
 329 understood. To examine this, we run the MEBM with the multi-model mean patterns of R_f and

330 G' , and confine the intermodel spread of λ to the tropics (30°S to 30°N) and polar regions (90°S to
331 30°S and 30°N to 90°N) while the other region is set to the multi-model mean of λ . This isolates
332 the impact of uncertainty in one region on $P' - E'$ uncertainty in other regions. Note that these
333 regions span equal areas of the globe.

334 Figure 6 shows the fractional contribution of intermodel variations of λ in the tropical and polar
335 regions to the total variance in $P' - E'$ for the same regions examined above. In the deep tropics
336 and subtropics, intermodel differences in tropical λ account for 85-92% of intermodel variance
337 in $P' - E'$. In the polar regions, intermodel differences in tropical λ contribute to approximately
338 30% of the intermodel variance in $P' - E'$. Notably, intermodel variations in λ in the polar regions
339 contribute little to intermodel variations in $P' - E'$ in the deep tropics and subtropics, but contribute
340 approximately 40% of the intermodel variations of $P - E$ in the extratropical polar regions. This
341 is similar to the results of Bonan et al. (2018), where tropical feedback uncertainty was found to
342 contribute to uncertainty in the amount of warming that was nearly uniform with latitude.

343 **4. Impact of radiative feedback patterns on hydrological changes**

344 Having shown that the MEBM emulates the pattern of $P' - E'$ simulated by GCMs under
345 greenhouse-gas forcing with high skill and that this pattern is largely determined by radiative
346 feedbacks, we now use the MEBM with idealized radiative-feedback patterns and a set of simple
347 scalings to investigate the specific mechanisms responsible for setting the $P' - E'$ pattern. We
348 construct a set of radiative-feedback patterns that isolate key differences between the MEBM and
349 HS06 approximation, to understand why the MEBM solution for $P' - E'$ performs better than the
350 HS06 approximation.

351 *a. Experiments and overview*

352 Because we showed that the pattern of radiative feedbacks contributes most to the intermodel
353 spread of $P' - E'$, we first set $G'(x) = 1.54 \text{ W m}^{-2}$ and $R_f(x) = 6.35 \text{ W m}^{-2}$, which are the multi-
354 model and global-mean values of the CMIP5 GCMs. D is set to $1.05 \times 10^6 \text{ m}^2 \text{ s}^{-1}$, which is the
355 multi-model mean value of the CMIP5 GCMs. We also take the multi-model mean climatological
356 MEBM variables (ψ , H , T) and make them symmetric about the equator. Thus, any asymmetries
357 in the analyses of Section 4 result from asymmetries in the pattern of radiative feedbacks only.

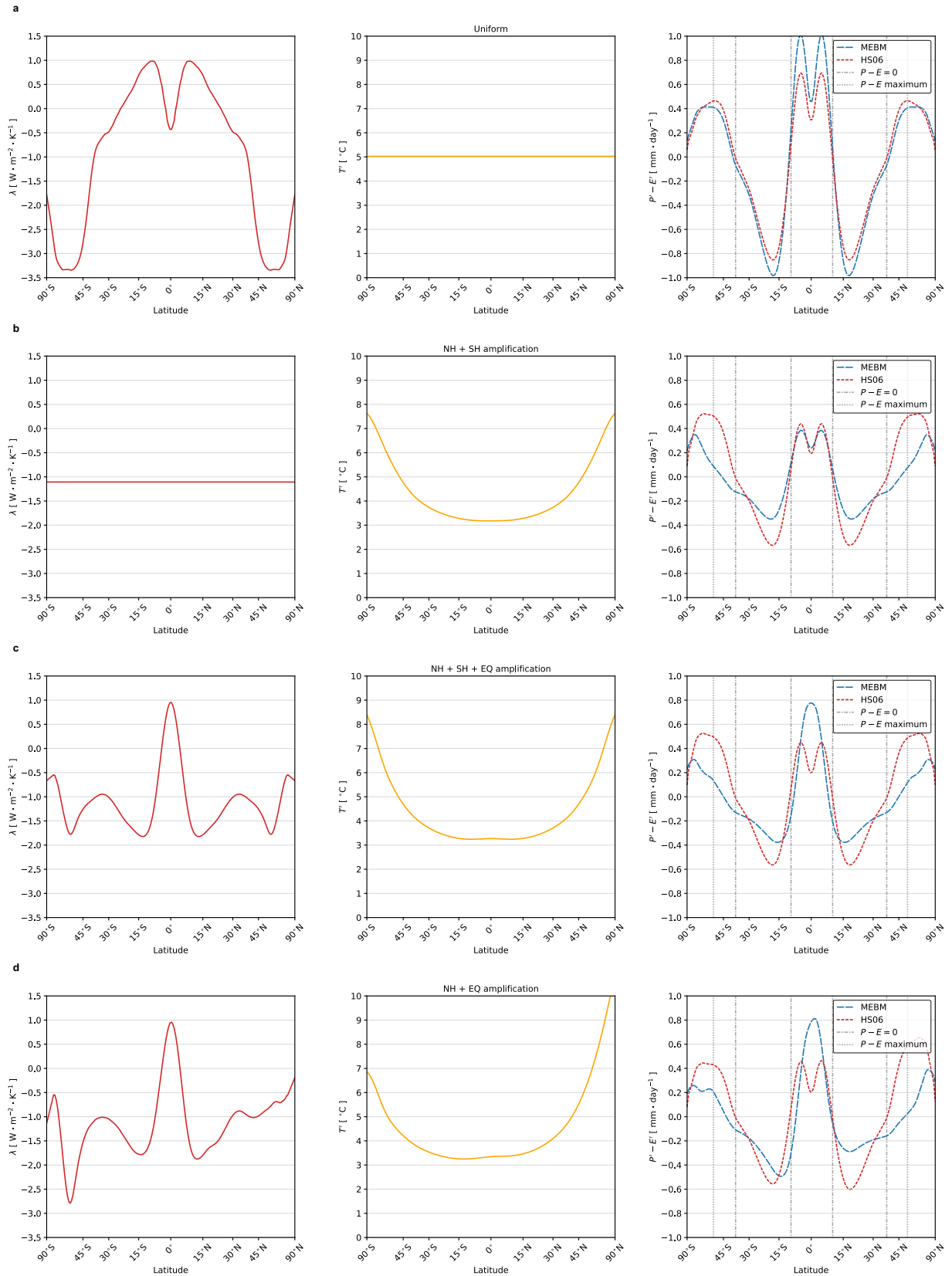


FIG. 7. See next page.

352 **FIG. 7. Impact of radiative feedback patterns on the response of the hydrological to global warming.** A
 353 (left) pattern of the net radiative feedback that induces a (middle) pattern of warming (a) that is uniform, (b)
 354 with equal degrees of polar amplification in the Northern Hemisphere and Southern Hemisphere, (c) with equal
 355 degrees of polar amplification in the Northern Hemisphere and Southern Hemisphere and amplified warming
 356 on the equator, and (d) with more polar amplification in the Northern Hemisphere than Southern Hemisphere
 357 and amplified warming on the equator. The right panel shows the pattern of $P' - E'$ for each pattern of the net
 358 radiative feedback. The blue dashed line denotes the MEBM solution and the red densely dashed line is the Held
 359 and Soden (2006) approximation assuming $\alpha = \% K^{-1}$ globally and using the multi-model mean climatological
 360 pattern of $P - E$ from 20 preindustrial control simulations, which is shown in Fig. 1c. Note that the climatological
 361 patterns have been symmetrized about the equator.

368 Next, we create four λ patterns that broadly represent the intermodel spread of CMIP5 GCMs and
 369 produce four distinct patterns of warming (Fig. 7). These patterns are as follows:

- 370 1. The first λ pattern is weakly negative in the deep tropics, positive in the subtropics, and
 371 negative in the extratropics (Fig. 7a). This λ pattern produces a pattern of warming that is
 372 uniform with latitude and equivalent to the multi-model and global-mean value of warming
 373 from the CMIP5 GCMs. This pattern was calculated by prescribing a uniform T' in Eq. (6)
 374 and solving for λ .
- 375 2. The second λ pattern is uniform with latitude and equivalent to the multi-model and global-
 376 mean value of λ from the CMIP5 GCMs (Fig. 7b). This λ pattern produces a pattern of
 377 warming that is polar-amplified in both hemispheres and contains little-to-no structure in the
 378 deep tropics.
- 379 3. The third λ pattern is symmetric across both hemispheres but contains a narrowly positive peak
 380 value of λ in the deep tropics and negative values elsewhere (Fig. 7c). This pattern was chosen
 381 to broadly represent the pattern of λ from GCMs that exhibit the largest increases in $P - E$ in
 382 the deep tropics. This λ pattern produces a pattern of warming that is also polar-amplified in
 383 both hemispheres, but contains a slight amplification of warming near the equator.
- 384 4. The fourth λ pattern is antisymmetric across both hemispheres but still contains a narrowly
 385 positive peak value of λ in the deep tropics and negative values elsewhere (Fig. 7d). This
 386 λ pattern produces a pattern of warming that is more polar-amplified in the Arctic and less

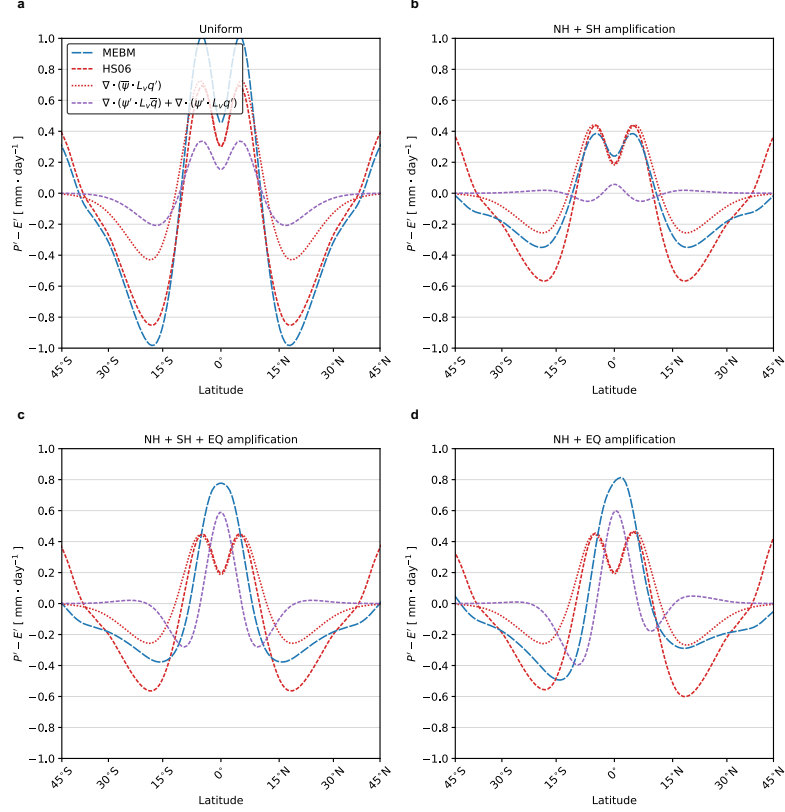
387 polar-amplified in the Antarctic, but also contains a slight amplification of warming near the
388 equator.

389 The resulting patterns of $P' - E'$ are shown in the right columns of Figure 7, along with a
390 comparison to the HS06 approximation. We briefly describe the patterns, before analyzing the
391 causes in the next two subsections, focusing separately on the tropics and extratropics. For Pattern
392 1, when λ is mostly positive in the subtropics and negative in the extratropics (Fig. 7a), the
393 pattern of warming is uniform. This results in a $P' - E'$ pattern that is nearly identical to the HS06
394 approximation (i.e., Eq. 4), with increasing $P - E$ in the tropics and high-latitudes and decreasing
395 $P - E$ in the subtropics. Note that this $P - E$ pattern contains no change in the subtropical boundaries
396 or narrowing of the ITCZ. However, for Pattern 2, when λ is uniform with latitude, there is a polar-
397 amplified pattern of warming, which results in a pattern of $P' - E'$ that is different between the
398 MEBM and HS06. For polar-amplified warming, while the pattern of $P' - E'$ for the MEBM and
399 HS06 approximation is similar in the tropics, $P' - E'$ in the extratropics and subtropics is much
400 more muted in the MEBM. Finally, for Pattern 3 and Pattern 4, when λ is narrowly positive in
401 the deep tropics and negative across most other latitudes, there is a similar difference between the
402 MEBM and HS06 $P' - E'$ in the high-latitudes, but the MEBM $P' - E'$ is larger in the deep tropics.
403 This increase in the deep tropics far exceeds the HS06 approximation (Eq. 4), and coincides with
404 a narrowing of the ITCZ where $P - E > 0$.

405 To provide a more mechanistic interpretation of how the pattern of λ impacts the pattern of
406 $P' - E'$, in the next two subsections we compare the MEBM and HS06 approximation using a set
407 of simple scalings.

408 *b. Tropics*

421 In Figure 1 and Figure 3 we saw that, in the tropics, $P' - E'$ in the MEBM is much larger than
422 $P' - E'$ in the HS06 approximation, and is in much better agreement with GCMs. This is also
423 evident in Figure 7 with the idealized radiative feedback patterns. These differences are likely
424 related to the MEBM containing a Hadley Cell parameterization that simulates changes to the
425 Hadley Cell circulation strength under warming. Thus, differences between the MEBM and HS06
426 approximation can be understood through the conservation statement for the atmospheric-moisture



409 **FIG. 8. Impact of radiative feedback patterns on the tropical hydrological cycle response.** The pattern
 410 of $P' - E'$ between 45°S and 45°N for a pattern of warming (a) that is uniform, (b) with equal degrees of
 411 polar amplification in the Northern Hemisphere and Southern Hemisphere, (c) with equal degrees of polar
 412 amplification in the Northern Hemisphere and Southern Hemisphere and amplified warming on the equator, and
 413 (d) with more polar amplification in the Northern Hemisphere than Southern Hemisphere and amplified warming
 414 on the equator. These are calculated following Section 4a (see Fig. 7). The blue dashed line denotes the MEBM
 415 solution. The red densely dashed line denotes the Held and Soden (2006) approximation assuming $\alpha = 7\%$
 416 K^{-1} globally. The red dotted line is the $P' - E'$ pattern with no circulation strength changes and changes to the
 417 moisture content of the atmosphere, $\nabla \cdot (\bar{\psi} L_v q')$. The purple dashed line is the $P' - E'$ pattern with circulation
 418 strength changes and changes to the moisture content of the atmosphere, $\nabla \cdot (\psi' L_v \bar{q}) + \nabla \cdot (\psi' L_v q')$. Note that
 419 the latitude range is confined to 45° as this is where the Hadley Cell parameterization begins to exhibit little-to-no
 420 influence on moisture transport.

427 budget for $P - E$ under warming:

$$(P' - E')_{\text{HC}} = -\nabla \cdot (\bar{\psi} L_v q' + \psi' L_v \bar{q} + \psi' L_v q'), \quad (14)$$

428 where $\overline{(\cdot)}$ represents the climatological state. Here, $\overline{\psi}$ and \overline{q} are derived by applying the MEBM
 429 to the each preindustrial control simulation from 20 GCMs (see Appendix B for details). This
 430 enables us to decompose $P' - E'$ in the MEBM — for regions where the Hadley Cell accomplishes
 431 most of the latent-energy transport — into thermodynamic and dynamic contributions to $P' - E'$.
 432 Broadly, the first term represents no changes to the strength of the Hadley Cell and changes to
 433 the moisture content of the atmosphere (which is nearly equivalent to Eq. 4); the second term
 434 represents changes to the strength of the Hadley Cell and no changes to the moisture content of the
 435 atmosphere; and the third term is second-order and combines changes to the strength of the Hadley
 436 Cell and moisture changes.

437 Figure 8 shows $P' - E'$ for each pattern of λ into contributions from the three terms in Eq. (14),
 438 in the region influenced by the Hadley Cells (45°S to 45°N). Under a uniform pattern of warming
 439 (Fig. 8a) the thermodynamic term (red dotted line) dominates $P' - E'$ while the two dynamical
 440 terms (purple line) simply amplify the existing pattern of $P - E$, with no change in the spatial
 441 structure of $P - E$. Note that the thermodynamic term, which does not represent changes to the
 442 strength of the Hadley Cell, is nearly equivalent to the HS06 approximation in the deep tropics.
 443 Similarly, under a pattern of warming with equal degrees of polar amplification in each hemisphere
 444 and uniform warming throughout the tropics (Fig. 8b), the thermodynamic term (red dotted line)
 445 again dominates $P' - E'$ and there is little-to-no change in the spatial pattern of $P - E$ in the deep
 446 tropics from the dynamical terms (purple line). However, under a pattern of warming with equal
 447 degrees of polar amplification in each hemisphere (Fig. 8c), but more warming near the equator,
 448 the dynamical terms dominate $P - E$ changes in the deep tropics. Here, ψ' causes an enhancement
 449 of $P - E$ in the deep tropics. Between 5°S and 5°N, changes to ψ contribute to an enhancement
 450 of approximately 5 mm day⁻¹ in $P - E$. Likewise, under amplified warming of the Arctic, more
 451 muted Southern Hemisphere warming, and amplified warming near the equator (Fig. 8d), there is
 452 larger $P - E$ in the deep tropics, which also arises mainly from changes in ψ .

453 Because the Hadley Cells greatly impact $P' - E'$ in the deep tropics, we now focus on the
 454 mechanisms responsible for the changes in circulation strength. To do this, we turn to Eq. (10),
 455 which relates the strength of the Hadley Cell in the MEBM to the poleward heat flux and gross

456 moist stability. Rearranging for $\psi'(x)$ gives:

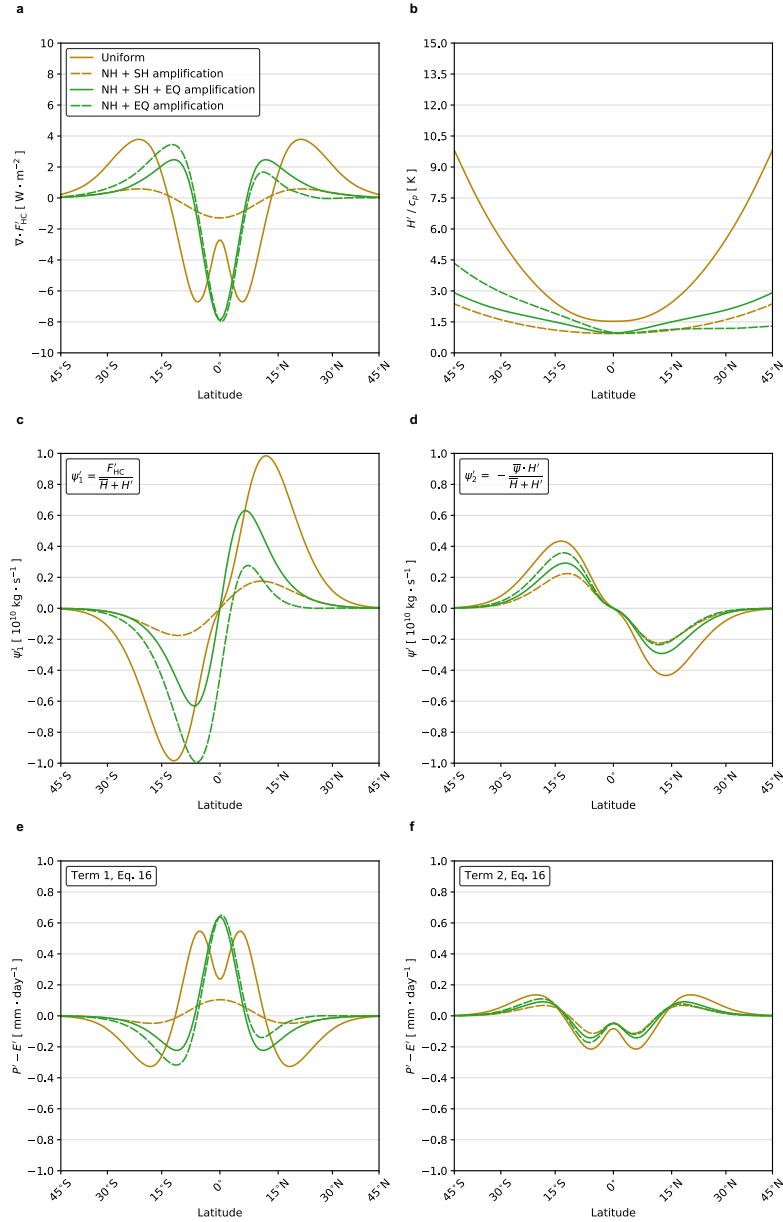
$$\psi'(x) = \underbrace{\frac{F'_{\text{HC}}}{\bar{H} + H'}}_{\psi'_1} - \underbrace{\frac{\bar{\psi}H'}{\bar{H} + H'}}_{\psi'_2} \quad (15)$$

457 where ψ'_1 represents changes to ψ that result from changes in the poleward heat transport by the
 458 Hadley Cell and ψ'_2 represents changes to ψ that result from changes in gross moist stability, or the
 459 stratification of the tropical atmosphere. Note that gross moist stability always scales at 8% above
 460 the equator value of h' , but can change due to changes in h' . These two terms can be combined
 461 with Eq. (14) to produce:

$$(P' - E')_{\text{HC}} = -\nabla \cdot \left(\bar{\psi}L_vq' + \underbrace{(\psi'_1L_v\bar{q} + \psi'_1L_vq')}_{\text{Term 1}} + \underbrace{(\psi'_2L_v\bar{q} + \psi'_2L_vq')}_{\text{Term 2}} \right) \quad (16)$$

462 where now $P' - E'$ can be decomposed into three terms: a thermodynamic term with no circulation
 463 strength changes but changes to the moisture content of the atmosphere (i.e., Eq. 4), and two
 464 dynamic terms that represent circulation strength changes from either the poleward heat transport
 465 by the Hadley Cell (Term 1) or changes in gross moist stability (Term 2).

474 Figure 9 shows the divergence of anomalous atmospheric heat transport (Fig. 9a) and anomalous
 475 gross moist stability (Fig. 9b) for each of the four λ patterns. These two variables can be used to
 476 decompose changes to the Hadley Cell circulation strength into the two terms from Eq. (15) (see
 477 Fig. 9c-d). The decomposition shows that changes to the poleward heat transport by the Hadley
 478 Cell (i.e., Term 1) largely act to strengthen ψ and that changes to gross moist stability (i.e., Term
 479 2) largely act to weaken of ψ (Fig. 9). With a pattern of λ that produces uniform warming there is
 480 excess energy in the tropics that must be exported poleward (see solid gold line in Fig. 9a), driving
 481 a stronger ψ (see solid gold line in Fig. 9c). Uniform warming also acts to produce the largest
 482 gross moist stability changes (see solid gold line in Fig. 9b), which weakens ψ (see solid gold
 483 line in Fig. 9d). However, there is no change in the spatial structure of ψ' and therefore $P' - E'$
 484 increases largely following the climatological state (see solid gold line in Fig. 9e-f). This is also



466 **FIG. 9. Mechanisms for the influence of radiative feedbacks on the tropical hydrological cycle response.**
 467 Changes to (a) the divergence of atmospheric energy transport by the Hadley Cells ($\nabla \cdot F'_{HC}$) and (b) gross moist
 468 stability (H'). Changes to the southward mass transport by the parameterized Hadley Cells, which is the sum of
 469 changes due (c) to the net atmospheric energy transport and (d) to gross moist stability changes. $P - E$ changes (e)
 470 from Term 1 and (f) Term 2 from (c) and (d), respectively (see Eq. 16). The gold solid line denotes the uniform
 471 warming case. The gold dashed line denotes the polar-amplified warming case. The purple solid line denotes
 472 the polar-amplified warming and Equator warming case. The purple dashed line denotes the Arctic-amplified
 473 warming and Equator warming case.

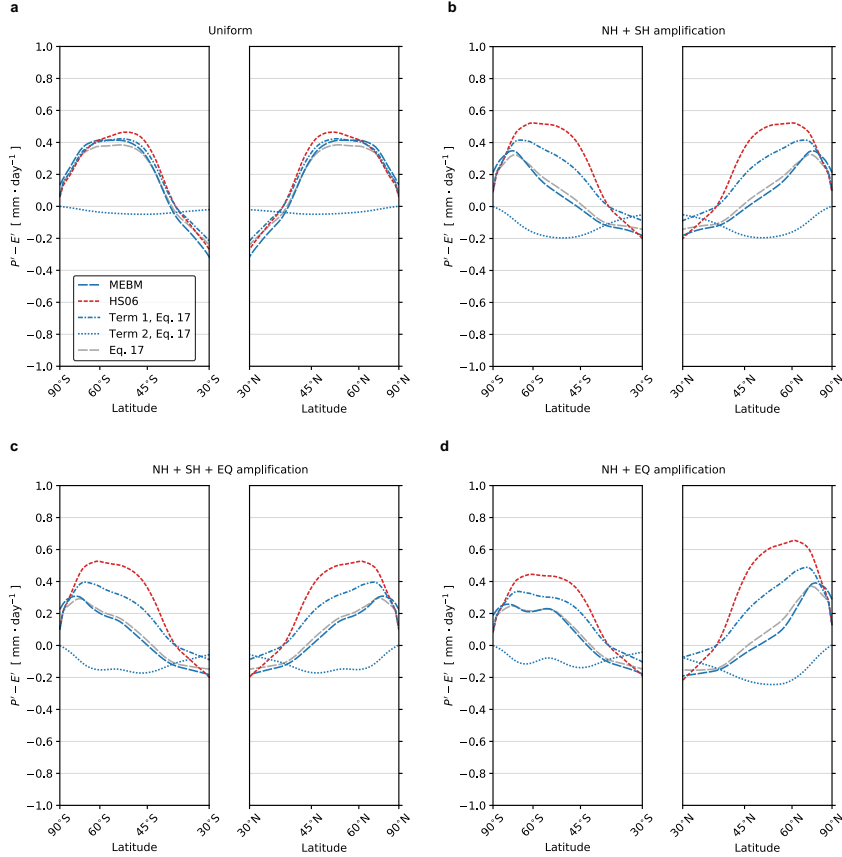
485 true for a uniform pattern of λ , where there are smaller changes to ψ , but again little-to-no change
486 to the spatial structure of ψ (see dashed gold line in Fig. 9c-d).

487 With a pattern of λ that is less negative in the tropics and much more narrowly peaked — which
488 is similar to the patterns of λ in GCMs — a different story emerges. Here, the small bump in
489 warming in the deep tropics leads to an excess of energy in the deep tropics (see green lines in Fig.
490 9a). This drives a stronger Hadley Cell in the deep tropics because of an increasing poleward heat
491 flux (see green lines in Fig. 9c). The excess energy cannot be radiated away locally and must be
492 exported to higher-latitudes, or regions of more efficient radiative loss. However, the structure of
493 λ determines where this energy can go and hence the response of ψ : strengthening ψ in the deep
494 tropics and weakening ψ in the subtropics (see green lines Fig. 9c). The fact that the λ peaks near
495 the equator and tapers off toward the subtropics means that ψ strengthens slightly more in the deep
496 tropics relative to the subtropics, helping to change its spatial structure (Fig. 9c). Furthermore,
497 because R_f and G' are spatially uniform, any spatial structure in λ must be balanced by the spatial
498 structure of $\nabla \cdot F'_{\text{HC}}$ or T' . And because $\nabla \cdot F'_{\text{HC}}$ contains more spatial structure than T' , the pattern
499 of λ ultimately drives the $P - E$ changes through the pattern of $\nabla \cdot F'_{\text{HC}}$. The change to the spatial
500 structure of ψ acts to increase $P - E$ in the deep tropics and decrease $P - E$ in the subtropics, which
501 narrows the ITCZ region (Fig. 9e).

502 Term 2, which represents changes to ψ from gross moist stability changes, is small and cannot
503 oppose the changes to ψ' in the deep tropics that results from changes to the poleward heat transport
504 by the Hadley Cell (Fig. 9d). However, in the subtropics the weakening of ψ out competes the
505 strengthening of ψ from an increase poleward heat flux (compare Fig. 9c and Fig. 9d). The
506 weakening, rather than strengthening, of ψ acts to decrease $P - E$ in the deep tropics (Fig.
507 9f). Together, in unison, the pattern of radiative feedbacks in the deep tropics and high-latitudes
508 determine the degree of ITCZ contraction through changes in the poleward heat transport by the
509 Hadley Cell and gross moist stability changes. These change are similar to Feldl and Bordoni
510 (2016), where the Hadley cell was found to strengthen and weaken under warming.

511 *c. Extratropics*

524 In the extratropics, $P' - E'$ from the MEBM and the HS06 approximation are approximately equal
525 under uniform warming (Fig. 7a), but are different under polar-amplified warming (Fig. 7b-d).



512 **FIG. 10. Impact of radiative feedback patterns on the extratropical hydrological cycle response.** The
 513 pattern of $P' - E'$ poleward of 30°S and 30°N for a pattern of warming: (a) that is uniform; (b) with equal degrees
 514 of polar amplification in the Northern Hemisphere and Southern Hemisphere; (c) with equal degrees of polar
 515 amplification in the Northern Hemisphere and Southern Hemisphere and amplified warming on the equator; and
 516 (d) with more polar amplification in the Northern Hemisphere than Southern Hemisphere and amplified warming
 517 on the equator (see Fig. 7). These are found following Section 4a (see Fig. 7). The blue dashed line denotes
 518 the MEBM solution. The red densely dashed line denotes the Held and Soden (2006) approximation assuming
 519 $\alpha = 7\% \text{ K}^{-1}$ globally. The blue dash-dotted line is the $P' - E'$ pattern from term one in Eq. (17), which represents
 520 changes to moisture content of the atmosphere with no changes to the transport of moisture. The blue dotted line
 521 is the $P' - E'$ pattern from term two in Eq. (17), which represents changes to the transport of moisture under
 522 warming. The grey dashed line is the $P' - E'$ pattern with transport changes included in addition to the full
 523 spatial structure of β (Eq. 17).

526 Under polar-amplified warming the MEBM predicts less enhancement of high-latitude $P - E$ than
 527 HS06, and is in better agreement with the GCMs (see Fig. 1a and Figs. 3). The MEBM also

528 predicts an expansion of the subtropical regions (see Section 1 and 3). To understand how these
 529 differences arise, we use an extended version of the simple scaling from HS06, which is detailed
 530 in Siler et al. (2018). Appendix C contains relevant details of the derivation, but this scaling
 531 decomposes $P' - E'$ in the extratropics into two terms via:

$$P' - E' = \underbrace{\beta(P - E)}_{\text{Term 1}} - \underbrace{\frac{1}{2\pi a^2} F_L \frac{d\beta}{dx}}_{\text{Term 2}}, \quad (17)$$

532 where:

$$\beta = \left(\alpha - \frac{2}{T} \right) T' + \frac{dT'/dx}{dT/dx}. \quad (18)$$

533 Eq. (17) implies that the pattern of $P' - E'$ is amplified under global warming by a factor of $\beta(x)$.
 534 Term 1 represents changes to the moisture content of the atmosphere, while Term 2 represents
 535 changes to the poleward moisture transport by eddies. HS06 argue that Eq. (17) can be simplified
 536 to Eq. (4) by ignoring changes in the pattern of warming, which means that β is approximately
 537 uniform and thus Term 2 in Eq. (17) is close to zero, making $P' - E' \approx \beta(P - E) = \alpha T'(P - E)$,
 538 or exactly Eq. (4). These arguments make sense for uniform warming, which indeed leads to
 539 Term 2 in Eq. (17) being close to zero and the structure of $P' - E'$ is simply the existing pattern
 540 of $P - E$ amplified by the pattern of warming, which is consistent with Fig. 7c. However, under
 541 polar-amplified warming these arguments make less sense, as strong meridional variations in T'
 542 act to alter both Term 1 and Term 2.

543 Figure 10 shows a decomposition of $P' - E'$ for each pattern of λ in the Northern and Southern
 544 Hemisphere extratropics (poleward of 30°) using the two terms in Eq. (17), the MEBM solution,
 545 and the HS06 approximation from Figure 7. Under uniform warming, where the MEBM and HS06
 546 approximation are approximately equal, the contribution of changes to the poleward moisture
 547 transport is relatively small (Fig. 10a). This occurs because $dT'/dx = 0$, making β relatively
 548 uniform and thus the transport of moisture (i.e., Term 2 in Eq. 17) is close to zero and contributes
 549 little to $P' - E'$. However, under polar-amplified warming the MEBM and HS06 approximation
 550 diverge because of changes to spatial structure of β and changes to the poleward moisture transport
 551 (Fig. 10b-d). Because T' increases with latitude, the meridional temperature gradient weakens and
 552 therefore β decreases everywhere, which partially offsets the Clausius-Clapeyron effect. A similar

553 feature is seen in under an asymmetric pattern of warming (Fig. 10d). When warming is amplified
554 mainly in the Arctic, there is a reduction of $P' - E'$ equal to approximately 2 mm year^{-1} uniformly
555 in the Northern Hemisphere extratropics. This decrease in poleward moisture transport reduces
556 the enhancement of $P' - E'$ in the high latitudes, and brings the MEBM in line with results from
557 GCMs.

558 *d. Connection to CMIP5 hydrological changes*

559 Armed with a better understanding of processes that set the pattern of $P' - E'$ in the tropics and
560 extratropics, we now revisit the ability of the MEBM to emulate comprehensive GCMs in CMIP5
561 using the same scalings from the previous sections.

562 1) TROPICAL HYDROLOGICAL CHANGES

570 Figure 11 shows a decomposition of $P' - E'$ associated with the three terms of Eq. (14),
571 which detail thermodynamic and dynamic changes to $P - E$ under warming. This is the same
572 decomposition shown in Figure 8, but for each individual GCM. Across most GCMs, changes to ψ
573 are large and have a large impact on the $P - E$ changes in the deep tropics. The change in ψ results
574 in enhancement of $P - E$ in the deep tropics. Between 5°S and 5°N , changes to ψ contribute to
575 an enhancement of approximately 6 mm day^{-1} in $P - E$. In GCMs with larger $P - E$ changes in
576 the deep tropics (e.g., ACCESS1.0 and MIROC-ESM), $\nabla \cdot (\psi' L_v \bar{q})$ and $\nabla \cdot (\psi' L_v q')$ contributes to
577 $8 - 9 \text{ mm day}^{-1}$ in $P - E$ changes. Conversely, in GCMs with smaller $P - E$ changes in the deep
578 tropics (e.g., CCSM4 and INM-CM4), $\nabla \cdot (\psi' L_v \bar{q})$ and $\nabla \cdot (\psi' L_v q')$ contributes $3 - 4 \text{ mm day}^{-1}$ in
579 $P - E$ changes. Additionally, GCMs with stronger hemispheric asymmetry in subtropical drying
580 (e.g., GFDL-ESM2M, HadGEM2-ES) exhibit this asymmetry because of two dynamical terms.

581 Indeed, $P - E$ changes in the deep tropics are significantly impacted by changes in circulation
582 strength. The mechanism for this is detailed in Figure 9 and due to the fact that some GCMs exhibit
583 a narrowly peaked pattern of less negative or even positive feedback values in the deep tropics near
584 the equator. This radiative feedback pattern implies more strengthening of ψ around the equator
585 and less strengthening (or weakening) of ψ in the subtropics, thereby changing the spatial structure
586 of ψ . In fact, the average feedback value in the deep tropics (averaged between 5°S and 5°N) is
587 strongly correlated ($r = 0.68$) with the $P' - E'$ values between 5°S and 5°N . Similarly, the average

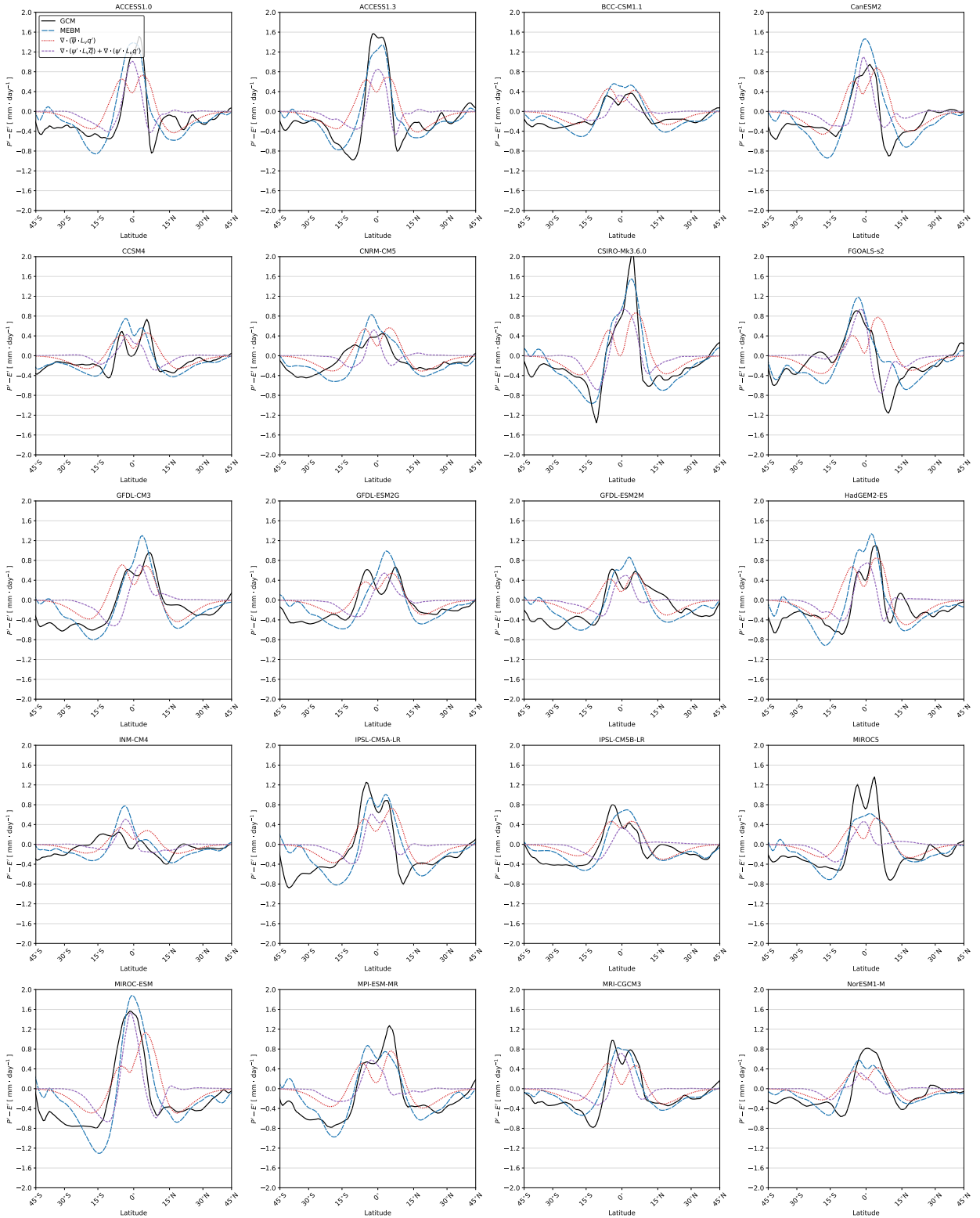


FIG. 11. See next page.

563 FIG. 11. **Tropical hydrological changes in CMIP5.** The pattern of $P' - E'$ between 45°S and 45°N for each
564 GCM. The black line denotes the GCM. The blue dashed line denotes the MEBM solution. The red dotted line
565 is the $P' - E'$ pattern from the MEBM with no circulation strength changes and changes to the moisture content
566 of the atmosphere, $\nabla \cdot (\bar{\psi} L_v q')$. The purple dashed line is the $P' - E'$ pattern from the MEBM with circulation
567 strength changes and changes to the moisture content of the atmosphere, $\nabla \cdot (\psi' L_v \bar{q}) + \nabla \cdot (\psi' L_v q')$. Note that the
568 latitude range is confined to 45° as this is where the Hadley Cell parameterization begins to exhibit little-to-no
569 influence on moisture transport.

588 divergence of the northward column-integrated atmosphere energy transport averaged between 5°S
589 and 5°N is also strongly correlated ($r = 0.72$) with the $P' - E'$ values between 5°S and 5°N. This
590 suggests the importance of radiative feedbacks in setting poleward heat transport, which acts to
591 strengthen the Hadley Cell circulation in the deep tropics and enhance $P - E$.

592 2) EXTRATROPICAL HYDROLOGICAL CHANGES

598 Figure 12 shows a decomposition of $P' - E'$ poleward of 30° into the two terms from Eq. (17),
599 which represent changes to the moisture content of the atmosphere and changes to the poleward
600 moisture flux. This is the same decomposition shown in Figure 10, but for each individual GCM.
601 Across all GCMs it is evident that reduced poleward moisture transport helps to align the MEBM
602 with GCMs. The poleward moisture transport (i.e., Term 2) decreases in both hemispheres across
603 most GCMs and accounts for 1 – 2 mm day⁻¹ decrease in $P - E$. The reduced poleward moisture
604 transport also causes the expansion of the subtropics in each GCM, which is shown by increasing
605 the latitude of $P - E = 0$. While not shown in Figure 12, GCMs with a stronger polar amplification
606 tend to have a stronger reduction in the poleward moisture transport, and stronger subtropical
607 drying.

608 5. Discussion and conclusions

609 Changes to the net water flux into the surface (i.e., $P - E$) are predicted to impact ecosystems
610 and socioeconomic activities throughout the world. While it is expected that, broadly, dry regions
611 will get drier and wet regions will get wetter, the magnitude and spatial structure of $P - E$ changes
612 remains uncertain. In this paper, we examined the response of $P - E$ to warming using a modified
613 MEBM that reroutes moisture transport in the deep tropics with a Hadley-Cell parameterization

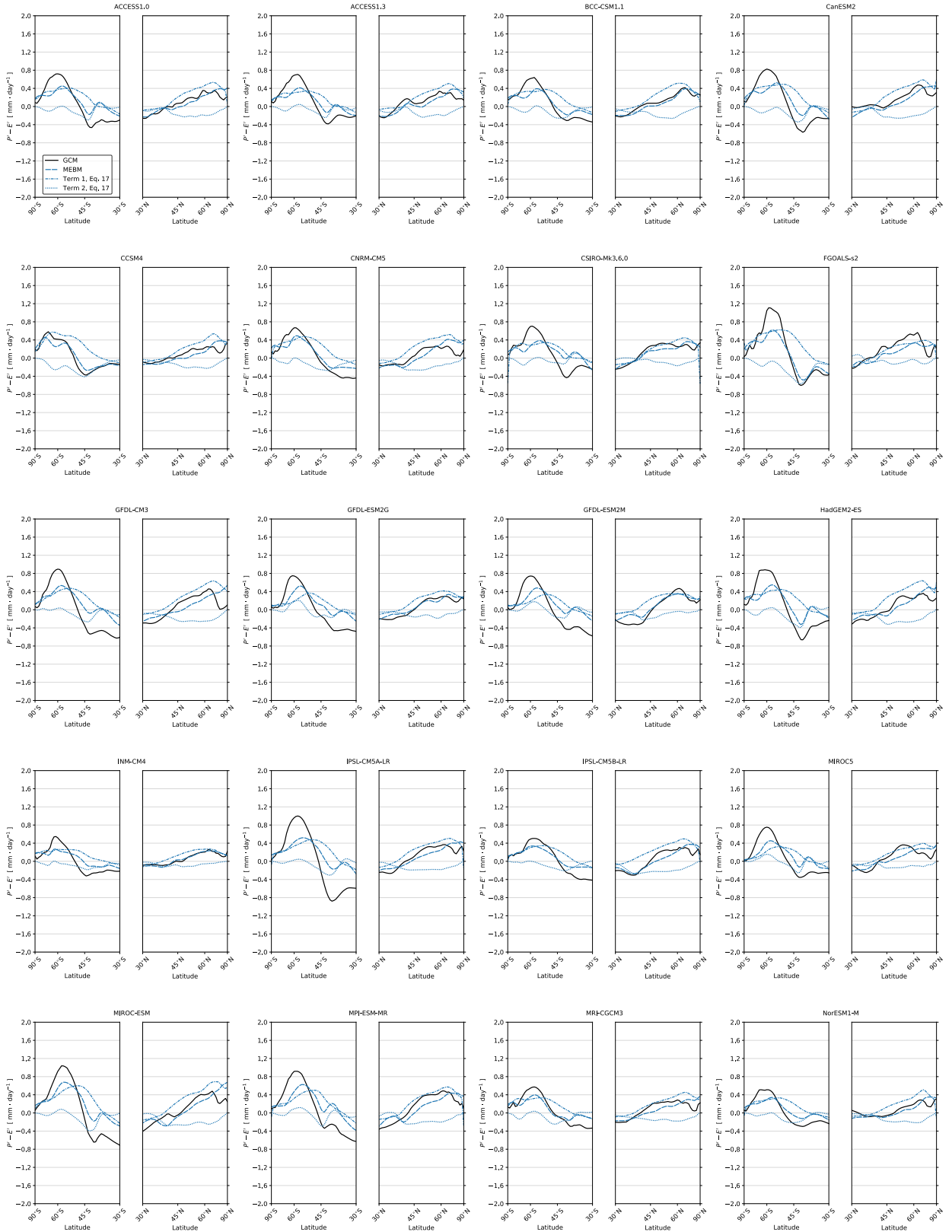


FIG. 12. See next page.

593 FIG. 12. **Extratropical hydrological changes in CMIP5.** The pattern of $P' - E'$ poleward of 30° . The black
594 line denotes the GCM response. The blue dashed line denotes the MEBM solution. The blue dash-dotted line is
595 the $P' - E'$ pattern from term one in Eq. (17) using MEBM output, which represents changes to moisture content
596 of the atmosphere with no changes to the transport of moisture. The blue dotted line is the $P' - E'$ pattern from
597 term two in Eq. (17) using MEBM output, which represents changes to the transport of moisture under warming.

614 (Siler et al. 2018). We showed that the MEBM accurately emulates $P - E$ change and accounts for
615 a majority of the intermodel variance in $P - E$ changes as simulated by GCMs under greenhouse-
616 gas forcing. We then used the MEBM to identify sources of uncertainty in the pattern of $P' - E'$
617 under warming. Using zonal-mean patterns of radiative forcing R_f , ocean heat uptake G' , and
618 the net radiative feedback λ from a suite of GCMs under $4 \times \text{CO}_2$, we showed that the MEBM
619 accounts for the majority of the intermodel variance in $P - E$ in the deep tropics, subtropics, and
620 extratropical high-latitudes. The intermodel spread in $P' - E'$ in these regions arises primarily
621 from intermodel differences in λ , with R_f and G' playing secondary roles. However, in regions
622 where regional ocean circulation shapes the rate of warming, G' can account for 30–40% of the
623 intermodel variance in $P - E$ changes. Finally, by confining the intermodel spread of λ to different
624 regions, we showed that intermodel variations of tropical λ impact $P - E$ change globally, whereas
625 intermodel variations of polar λ mainly impact $P - E$ changes in the poles.

626 Motivated by the fact that radiative feedbacks play a leading role in setting the pattern of $P - E$, we
627 constructed a set of idealized radiative feedback patterns and used some extended scalings to further
628 investigate processes impacting $P' - E'$. We demonstrated that $P - E$ changes depends crucially on
629 the meridional pattern of warming and the net energy input into the atmosphere. Under uniform
630 warming, $P - E$ changes occurs at a rate approximately equal to the Clausius-Clapeyron, consistent
631 with the thermodynamic scaling first introduced by Held and Soden (2006). However, under polar-
632 amplified warming, moisture transport to the high-latitudes decreases causing less of an increase
633 in $P - E$ in the high-latitudes. Interestingly, when the net energy input into the atmosphere is large
634 near the equator and begins to taper off in the subtropics, $P - E$ in the deep tropics increases and the
635 ITCZ region narrows. This occurs because the large net energy input into the atmosphere cannot
636 be radiated away locally at the equator, which means the circulations must strengthen locally to
637 transport that excess energy away. This changes the spatial structure of the Hadley Cell circulation
638 strength and causes a convergence of moisture in the deep tropics, increasing $P - E$ in the tropics

639 and decreasing $P - E$ in the subtropics. Finally, under asymmetric warming, where warming is
640 more amplified in the Arctic when compared to the Antarctic, but there is still a slight amplification
641 of tropical warming, we find a similar reduction in poleward moisture transport and narrowing
642 of the ITCZ region, but the subtropics dry less in the Northern Hemisphere when compared to
643 the Southern Hemisphere. This mimics the hemispheric asymmetry of subtropical drying seen
644 in GCMs and is traced to the asymmetric response of the changing atmospheric circulation.
645 These circulation strength changes can be understood as a consequence of the demands of overall
646 downgradient energy transport, as encapsulated in the MEBM.

647 Our study has several implications. Given the role of polar amplification in setting the magnitude
648 of the poleward moisture flux, the processes that set Arctic amplification — which is quite uncertain
649 across GCMs (Pithan and Mauritsen 2014; Bonan et al. 2018; Feldl et al. 2020) — may also explain
650 uncertainty in $P - E$ changes, particularly for the Northern Hemisphere extratropics. Similarly,
651 the relative warming of the Arctic versus the Antarctic, and the processes contributing to this
652 asymmetry may explain intermodel differences in the amount of subtropical drying between each
653 hemisphere by affecting the poleward heat flux and thus the strength of the Hadley Cell circulation.
654 Furthermore, the role that radiative feedbacks play in setting $P - E$ changes under warming suggests
655 that studying the effect of each individual radiative feedback may help identify limits to the “wet gets
656 wetter, dry gets drier” paradigm and offer insights into potential biases in GCMs. Finally, our results
657 indicate that changes to large-scale tropical circulations can be energetically-constrained with a
658 simple rule of downgradient energy transport, and that this rule helps to explain the narrowing
659 of the ITCZ and hemispheric asymmetry in subtropical drying. Understanding how energetic
660 constraints can be used to understand other dynamical features in GCMs (e.g., Feldl and Bordoni
661 2016) should be explored in further detail.

662 This study, however, contains a few caveats. In the MEBM the spatial patterns of R_f , λ , and
663 G' are prescribed and do not change over time. Thus, we are unable to consider transient $P - E$
664 changes under global warming and the extent to which the spatial patterns of λ and G' are truly
665 independent of atmospheric heat and moisture transport. Additionally, the assumption that D is
666 spatially uniform and invariant under warming is surely a crude approximation. Previous work
667 has shown that D can be approximately 75% larger in the mid-latitudes when compared to the
668 subtropics (Frierson et al. 2007; Peterson and Boos 2020) and can affect the degree of meridional

669 shifts in tropical rainfall (Peterson and Boos 2020). D has also been shown to decrease under
670 sustained greenhouse-gas forcing (Shaw and Voigt 2016; Mooring and Shaw 2020). Future work
671 might explore how more accurate patterns of D , which account for changing atmospheric dynamics,
672 impact the results of this study. Finally, because we fix the Gaussian weighting function $w(x)$, our
673 results do not account for changes between latent-energy transport accomplished by midlatitude
674 eddies and the Hadley Cell. Future work might also explore a version of a MEBM where $w(x)$ is
675 a function of the climate state, or where $w(x)$ accounts for extratropical mean circulations such as
676 the Ferrel or polar cells.

677 Despite these shortcomings, the fact that the MEBM emulates $P - E$ changes as simulated in
678 GCMs under greenhouse-gas forcing, suggests that the MEBM and the processes it represents offers
679 a parsimonious understanding of the causes of hydrological change that is distinct from the simple
680 thermodynamic scaling that results in the “wet gets wet, dry gets drier” paradigm. Specifically,
681 in this paper, we showed how the MEBM captures changes to the transport of moisture to the
682 high-latitudes and changes to tropical $P - E$ through energetically-constrained Hadley Cells. This
683 work demonstrates that the spatial structure of radiative feedbacks can greatly impact changes
684 to the strength of the Hadley Cell circulation, acting to narrow the ITCZ and increase $P - E$
685 in the deep tropics. This work also demonstrates the utility of downgradient energy transport
686 to examine drivers of the intermodel spread in $P - E$ changes. Our results suggest that, for
687 as long as tropical feedbacks and polar amplification remain uncertain and poorly constrained
688 among GCMs, projections of the spatial pattern of hydrological change will also remain uncertain.
689 Thus, downgradient energy transport and energetic constraints on the strength of the Hadley Cell
690 circulation provide an alternative and perhaps more fundamental explanation for the response of
691 $P - E$ to climate change.

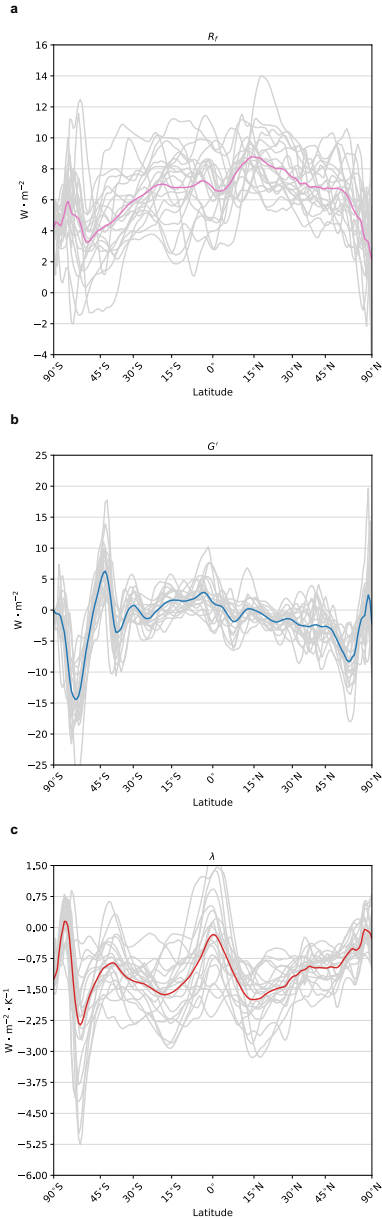
692 APPENDIX A

693 CMIP5 output

694 We use monthly output from 20 different GCMs participating in Phase 5 of the Coupled Model
695 Intercomparison Project (CMIP5; Taylor et al. 2012). This subset of GCMs reflects those that
696 provide the necessary output for calculating $R_f(x)$, $G'(x)$, and $\lambda(x)$. For each GCM, we calculate
697 anomalies in each variable, denoted by prime, as the difference between the variable averaged

698 over a preindustrial control simulation and the variable averaged over the last 25 years of $4 \times \text{CO}_2$
699 simulations (years 126 – 150). All variables are annual- and zonal- means computed from monthly
700 output. The variables include: all-sky shortwave and longwave radiation at the surface and top of
701 atmosphere (rsds, rsus, rsdt, rsut, rlds, rlus, rlut), sensible and latent heat fluxes (hfss, hfls), sea
702 surface temperature (tos), near-surface air temperature (tas), precipitation (pr), and evaporation
703 (evs).

704 $R_f(x)$ is calculated from the change in top of atmosphere (TOA) radiation in $4 \times \text{CO}_2$ simulations
705 performed with fixed preindustrial sea surface temperatures (Siler et al. 2019). $G'(x)$ is calculated
706 as the change in net surface heat fluxes in $4 \times \text{CO}_2$ simulations performed in fully coupled GCMs.
707 $\lambda(x)$ is calculated by equating the zonal-mean net TOA radiation anomaly with $\lambda(x)T'(x) + R_f(x)$.
708 Figure A1 shows the patterns of $R_f(x)$, $G'(x)$, and $\lambda(x)$ for each GCM.



709 **FIG. A1. Input to the moist energy balance model.** The zonal-mean profile of (a) radiative forcing (R_f),
 710 (b) ocean heat uptake (G'), and (c) the net radiative feedback (λ) from 20 CMIP5 GCMs 126 – 150 years after
 711 an abrupt quadrupling of CO_2 . The grey lines represent each individual GCM and the colored lines denote the
 712 multi-model mean.

APPENDIX B

Climatological Hadley Cell parameterization

In the main text, we introduce the Hadley Cell parameterization using the perturbation version of the MEBM. However, the mass transport of the Hadley Cell and thus the pattern of $P' - E'$ depends to some extent on the climatological state via Eq. (10) and Eq. (11). To account for this, we use a climatological version of the MEBM to estimate the climatological state of each GCM. This is done by first calculating the net heating of the atmosphere $Q_{\text{net}}(x)$, which is the difference between the net downward energy flux at the TOA and the surface in preindustrial control simulations (see Appendix A). Because the northward column-integrated atmospheric energy transport F is assumed to be related to the meridional gradient in h , the climatological version of the MEBM is:

$$Q_{\text{net}}(x) = -\frac{p_s}{a^2 g} D \frac{d}{dx} \left[(1-x^2) \frac{dh}{dx} \right]. \quad (\text{B1})$$

The MEBM climatological values of $T(x)$ and $q(x)$ (assuming relative humidity is fixed at 80%) can be found by minimizing the difference between the zonal-mean near-surface air temperature and Q_{net} from each GCM using Eq. B1. A similar procedure as described in Section 2 is then used to calculate $\psi(x)$, $H(x)$, and $P - E$ except that the poleward heat flux and moisture flux take the form of:

$$F_{\text{HC}}(x) = \psi(x)H(x), \quad (\text{B2})$$

and

$$F_{L,\text{HC}}(x) = \psi(x)L_v q(x), \quad (\text{B3})$$

respectively. Note that here D is unique to each GCM. For Section 3, the value of D is unique to each GCM and for Section 4, the value of D is $1.05 \times 10^6 \text{ m}^2 \text{ s}^{-1}$ (i.e., the multi-model mean value). For Section 3, the climatological variables are unique to each GCM and for Section 4, the climatological variables are the multi-model mean patterns and made to be symmetric about the equator.

APPENDIX C

Diffusive energy transport scaling

736 The scaling in Eq. (17) was first derived by HS06 and can be approximated through the following
 737 arguments. First, by assuming that moisture and temperature are diffused with the same diffusivity,
 738 the ratio of the latent-heat transport F_L to the sensible-heat transport F_S will be the ratio of the
 739 meridional gradient of $L_v q$ to the meridional gradient of $c_p T$, where c_p is the specific heat of air
 740 and q is near-surface specific humidity (assuming fixed relative humidity at 80%), meaning:

$$\frac{F_L}{F_S} = \frac{L_v}{c_p} \frac{dq}{dT}, \quad (\text{C1})$$

741 where

$$\frac{dq}{dT} = \frac{dq/dx}{dT/dx}, \quad (\text{C2})$$

742 and x is the sine of latitude. Because the Clausius-Clapeyron equation states that:

$$\frac{dq}{dT} = \alpha q, \quad (\text{C3})$$

743 the fractional change in the moisture transport under warming can be approximated as:

$$\frac{F'_L}{F_L} \approx \frac{(\alpha q)'}{\alpha q} + \frac{F'_S}{F_S}, \quad (\text{C4})$$

744 which can be re-arranged to be:

$$\frac{F'_L}{F_L} \approx \left(\alpha - \frac{2}{T} \right) T' + \frac{F'_S}{F_S}. \quad (\text{C5})$$

745 Thus, the change in moisture transport under warming can be written as:

$$F'_L(x) \approx \beta F_L(x), \quad (\text{C6})$$

746 where

$$\beta = \left(\alpha - \frac{2}{T} \right) T' + \frac{dT'/dx}{dT/dx}. \quad (\text{C7})$$

747 Note that the fractional change in sensible heat transport is now written in terms of the gradient in
 748 near-surface air temperature. Finally, the change in $P - E$ under warming can be found by taking

749 the divergence of Eq. (C6) which, together with Eq. (C7), results in:

$$P' - E' = \underbrace{\beta(P - E)}_{\text{Term 1}} - \underbrace{\frac{1}{2\pi a^2} F_L \frac{d\beta}{dx}}_{\text{Term 2}}. \quad (\text{C8})$$

750 Here, Term 1 represents changes to the moisture content of the atmosphere under warming and
751 Term 2 represents changes to the poleward moisture flux under warming. HS06 argue that the
752 dependence of the saturation vapor pressure on T and the fractional change of sensible-heat
753 transport in Eq. (C7) are small and can be ignored. They also argue that because the pattern
754 of warming is relatively uniform, the second term on the right hand side of Eq. (C8), which
755 represents changes to the transport of moisture, is close to zero. Removing these terms results in
756 $P' - E' = \beta(P - E) = \alpha T'(P - E)$, which is exactly Eq. (4). Thus, the difference between Eq. (4)
757 and Eq. (C8) results from the pattern of temperature change T' and the climatological pattern of
758 T , which determine the moisture content of the atmosphere and poleward moisture transport.

759 *Acknowledgments.* The authors thank Polina Khapikova for helpful comments on an earlier draft
760 of this paper. Part of this research was supported by the University of Washington Mary Gates
761 Endowment for Undergraduate Students. D.B.B was supported by an American Meteorologi-
762 cal Society (AMS) Graduate Fellowship and the National Science Foundation (NSF) Graduate
763 Research Fellowship Program (NSF Grant DGE1745301). N.S. was supported by NSF Grant
764 AGS-1954663. G.H.R. was supported by NSF Grants AGS-2019647 and P2C2-2102829. K.C.A.
765 was supported by NSF Grants AGS-1752796 and AGS-2019647, and an Alfred P. Sloan Research
766 Fellowship (Grant FG-2020-13568). We thank the climate modeling groups for producing and
767 making available their model output, which is accessible at the Earth System Grid Federation
768 (ESGF) Portal (<https://esgf-node.llnl.gov/search/cmip5/>).

769 *Data availability statement.* The data for this study will be made available upon acceptance at
770 <https://github.com/dbonan>.

771 **References**

772 Abernathey, R. P., I. Cerovecki, P. R. Holland, E. Newsom, M. Mazloff, and L. D. Talley, 2016:
773 Water-mass transformation by sea ice in the upper branch of the Southern Ocean overturning.

- 774 *Nature Geoscience*, **9** (8), 596–601.
- 775 Armour, K. C., N. Siler, A. Donohoe, and G. H. Roe, 2019: Meridional atmospheric heat transport
776 constrained by energetics and mediated by large-scale diffusion. *Journal of Climate*, **32** (12),
777 3655–3680.
- 778 Beer, E., and I. Eisenman, 2022: Revisiting the role of the water vapor and lapse rate feedbacks in
779 the Arctic amplification of climate change. *Journal of Climate*, 1–33.
- 780 Bonan, D. B., K. Armour, G. Roe, N. Siler, and N. Feldl, 2018: Sources of uncertainty in the
781 meridional pattern of climate change. *Geophysical Research Letters*, **45** (17), 9131–9140.
- 782 Boos, W. R., 2012: Thermodynamic scaling of the hydrological cycle of the Last Glacial Maximum.
783 *Journal of Climate*, **25** (3), 992–1006.
- 784 Byrne, M. P., and P. A. O’Gorman, 2015: The response of precipitation minus evapotranspiration
785 to climate warming: Why the “wet-get-wetter, dry-get-drier” scaling does not hold over land.
786 *Journal of Climate*, **28** (20), 8078–8092.
- 787 Byrne, M. P., and T. Schneider, 2016a: Energetic constraints on the width of the intertropical
788 convergence zone. *Journal of Climate*, **29** (13), 4709–4721.
- 789 Byrne, M. P., and T. Schneider, 2016b: Narrowing of the ITCZ in a warming climate: Physical
790 mechanisms. *Geophysical Research Letters*, **43** (21), 11–350.
- 791 Carmichael, M. J., and Coauthors, 2016: A model–model and data–model comparison for the early
792 Eocene hydrological cycle. *Climate of the Past*, **12** (2), 455–481.
- 793 Chang, E. K., Y. Guo, and X. Xia, 2012: CMIP5 multimodel ensemble projection of storm track
794 change under global warming. *Journal of Geophysical Research: Atmospheres*, **117** (D23).
- 795 Chou, C., and J. D. Neelin, 2004: Mechanisms of global warming impacts on regional tropical
796 precipitation. *Journal of climate*, **17** (13), 2688–2701.
- 797 Dai, A., and K. E. Trenberth, 2002: Estimates of freshwater discharge from continents: Latitudinal
798 and seasonal variations. *Journal of hydrometeorology*, **3** (6), 660–687.

799 de Boyer Montégut, C., J. Mignot, A. Lazar, and S. Cravatte, 2007: Control of salinity on the
800 mixed layer depth in the world ocean: 1. General description. *Journal of Geophysical Research:*
801 *Oceans*, **112** (C6).

802 Emori, S., and S. Brown, 2005: Dynamic and thermodynamic changes in mean and extreme
803 precipitation under changed climate. *Geophysical Research Letters*, **32** (17).

804 Feldl, N., and S. Bordoni, 2016: Characterizing the Hadley circulation response through regional
805 climate feedbacks. *Journal of Climate*, **29** (2), 613–622.

806 Feldl, N., S. Po-Chedley, H. K. Singh, S. Hay, and P. J. Kushner, 2020: Sea ice and atmospheric
807 circulation shape the high-latitude lapse rate feedback. *NPJ climate and atmospheric science*,
808 **3** (1), 1–9.

809 Field, C. B., and V. R. Barros, 2014: *Climate change 2014—Impacts, adaptation and vulnerability:*
810 *Regional aspects*. Cambridge University Press.

811 Flannery, B. P., 1984: Energy balance models incorporating transport of thermal and latent energy.
812 *Journal of the Atmospheric Sciences*, **41** (3), 414–421.

813 Frierson, D. M., I. M. Held, and P. Zurita-Gotor, 2007: A gray-radiation aquaplanet moist GCM.
814 Part II: Energy transports in altered climates. *Journal of the Atmospheric Sciences*, **64** (5),
815 1680–1693.

816 Groeskamp, S., S. M. Griffies, D. Iudicone, R. Marsh, A. G. Nurser, and J. D. Zika, 2019: The
817 water mass transformation framework for ocean physics and biogeochemistry. *Annual review of*
818 *marine science*, **11**, 271–305.

819 Held, I. M., 2001: The partitioning of the poleward energy transport between the tropical ocean
820 and atmosphere. *Journal of the Atmospheric Sciences*, **58** (8), 943–948.

821 Held, I. M., and B. J. Soden, 2006: Robust responses of the hydrological cycle to global warming.
822 *Journal of climate*, **19** (21), 5686–5699.

823 Hill, S. A., N. J. Burls, A. Fedorov, and T. M. Merlis, 2020: Symmetric and antisymmetric
824 components of polar-amplified warming. *arXiv preprint arXiv:2012.09228*.

- 825 Hwang, Y.-T., and D. M. Frierson, 2010: Increasing atmospheric poleward energy transport with
826 global warming. *Geophysical Research Letters*, **37** (24).
- 827 Kang, S. M., and J. Lu, 2012: Expansion of the Hadley cell under global warming: Winter versus
828 summer. *Journal of Climate*, **25** (24), 8387–8393.
- 829 Large, W. G., and A. G. Nurser, 2001: Ocean surface water mass transformation. *International*
830 *Geophysics*, Vol. 77, Elsevier, 317–336.
- 831 Liu, M., G. Vecchi, B. Soden, W. Yang, and B. Zhang, 2021: Enhanced hydrological cycle
832 increases ocean heat uptake and moderates transient climate change. *Nature Climate Change*,
833 **11** (10), 848–853.
- 834 Lu, J., G. Chen, and D. M. Frierson, 2010: The position of the midlatitude storm track and eddy-
835 driven westerlies in aquaplanet AGCMs. *Journal of Atmospheric Sciences*, **67** (12), 3984–4000.
- 836 Lu, J., G. A. Vecchi, and T. Reichler, 2007: Expansion of the Hadley cell under global warming.
837 *Geophysical Research Letters*, **34** (6).
- 838 Lutsko, N. J., J. T. Seeley, and D. W. Keith, 2020: Estimating Impacts and Trade-offs in Solar
839 Geoengineering Scenarios With a Moist Energy Balance Model. *Geophysical Research Letters*,
840 **47** (9), e2020GL087290.
- 841 Mbengue, C., and T. Schneider, 2013: Storm track shifts under climate change: What can be
842 learned from large-scale dry dynamics. *Journal of Climate*, **26** (24), 9923–9930.
- 843 Mbengue, C., and T. Schneider, 2017: Storm-track shifts under climate change: Toward a mecha-
844 nistic understanding using baroclinic mean available potential energy. *Journal of the Atmospheric*
845 *Sciences*, **74** (1), 93–110.
- 846 Mbengue, C., and T. Schneider, 2018: Linking Hadley circulation and storm tracks in a conceptual
847 model of the atmospheric energy balance. *Journal of the Atmospheric Sciences*, **75** (3), 841–856.
- 848 Merlis, T. M., and M. Henry, 2018: Simple estimates of polar amplification in moist diffusive
849 energy balance models. *Journal of Climate*, **31** (15), 5811–5824.
- 850 Mitchell, J., C. Wilson, and W. Cunnington, 1987: On CO₂ climate sensitivity and model depen-
851 dence of results. *Quarterly Journal of the Royal Meteorological Society*, **113** (475), 293–322.

852 Mooring, T. A., and T. A. Shaw, 2020: Atmospheric diffusivity: A new energetic framework for
853 understanding the midlatitude circulation response to climate change. *Journal of Geophysical*
854 *Research: Atmospheres*, **125** (1), e2019JD031 206.

855 O’Gorman, P. A., and T. Schneider, 2008: The hydrological cycle over a wide range of climates
856 simulated with an idealized GCM. *Journal of Climate*, **21** (15), 3815–3832.

857 Peterson, H. G., and W. R. Boos, 2020: Feedbacks and eddy diffusivity in an energy balance model
858 of tropical rainfall shifts. *npj Climate and Atmospheric Science*, **3** (1), 1–9.

859 Pithan, F., and T. Mauritsen, 2014: Arctic amplification dominated by temperature feedbacks in
860 contemporary climate models. *Nature geoscience*, **7** (3), 181–184.

861 Prein, A. F., and A. G. Pendergrass, 2019: Can we constrain uncertainty in hydrologic cycle
862 projections? *Geophysical Research Letters*, **46** (7), 3911–3916.

863 Roe, G. H., N. Feldl, K. C. Armour, Y.-T. Hwang, and D. M. Frierson, 2015: The remote impacts
864 of climate feedbacks on regional climate predictability. *Nature Geoscience*, **8** (2), 135–139.

865 Russotto, R. D., and M. Biasutti, 2020: Polar amplification as an inherent response of a circulating
866 atmosphere: results from the TRACMIP aquaplanets. *Geophysical Research Letters*, **47** (6),
867 e2019GL086 771.

868 Scheff, J., and D. Frierson, 2012: Twenty-first-century multimodel subtropical precipitation de-
869 clines are mostly midlatitude shifts. *Journal of Climate*, **25** (12), 4330–4347.

870 Schmitt, R. W., P. S. Bogden, and C. E. Dorman, 1989: Evaporation minus precipitation and
871 density fluxes for the North Atlantic. *Journal of Physical Oceanography*, **19** (9), 1208–1221.

872 Seager, R., N. Naik, and G. A. Vecchi, 2010: Thermodynamic and dynamic mechanisms for
873 large-scale changes in the hydrological cycle in response to global warming. *Journal of Climate*,
874 **23** (17), 4651–4668.

875 Seager, R., and G. A. Vecchi, 2010: Greenhouse warming and the 21st century hydroclimate
876 of southwestern North America. *Proceedings of the National Academy of Sciences*, **107** (50),
877 21 277–21 282.

- 878 Shaw, T. A., and A. Voigt, 2016: What can moist thermodynamics tell us about circulation shifts
879 in response to uniform warming? *Geophysical Research Letters*, **43** (9), 4566–4575.
- 880 Siler, N., G. H. Roe, and K. C. Armour, 2018: Insights into the zonal-mean response of the
881 hydrologic cycle to global warming from a diffusive energy balance model. *Journal of Climate*,
882 **31** (18), 7481–7493.
- 883 Siler, N., G. H. Roe, K. C. Armour, and N. Feldl, 2019: Revisiting the surface-energy-flux
884 perspective on the sensitivity of global precipitation to climate change. *Climate Dynamics*,
885 **52** (7), 3983–3995.
- 886 Taylor, K. E., R. J. Stouffer, and G. A. Meehl, 2012: An overview of CMIP5 and the experiment
887 design. *Bulletin of the American Meteorological Society*, **93** (4), 485–498.
- 888 Winguth, A., C. Shellito, C. Shields, and C. Winguth, 2010: Climate response at the Paleocene–
889 Eocene Thermal Maximum to greenhouse gas forcing—A model study with CCSM3. *Journal*
890 *of Climate*, **23** (10), 2562–2584.